Pt(111) Surface Preparation for Oxide Quasicrystal Thin-Film Growth

Harry Hibbert 200983774

May 11, 2018

A Thesis submitted in partial fulfilment of the requirements for the degree of

Bachelor of Science

Under the supervision of Dr. Hem Raj Sharma

At the

University of Liverpool Department of Physics

May 2018

Declaration

I hereby declare that this thesis is my own work and effort and that it has not been submitted anywhere for any award. Where other sources of information have been used, they have been acknowledged.

Signature .....

Abstract

A report into the preparation of a clean Pt(111) surface for the deposition of $BaTiO_3$ thin-film. On annealing the $BaTiO_3$ restructures into a quasicrystalline thin-film. The Pt(111) surface was cleaned with cycles of 10 minute 3keV Ar^+ sputtering and 20 minutes annealing at 650°C in an ultra high vacuum (UHV) environment. Scanning tunnelling microscope images were taken, along with low energy electron diffraction patterns. Analysis of terrace step heights in STM images confirmed the Pt's (111) orientation. Angles of diffraction were determined from the geometry of the experimental setup, the angles of diffraction were found to be consistent with the Bragg theory of diffraction, within the experiments region of error. The recorded diffraction pattern was consistent with a simulated diffraction pattern generated in the open source software LEED-pat4.

Contents

1 Introduction

Quasicrystals (QC) were discovered by Dan Schechtman in 1982 by observing a metallic solid using an electron microscope and x-ray diffraction which had long-range orientational order, but with icosahedral point group symmetry, which was inconsistent with lattice translations. Schechtman noted that a crystal should not be able to exhibit icosahedral point group symmetry. The metallic solid observed had diffraction spots which could not be indexed to any Bravais lattice [1]. Crystal structures are highly ordered with long range orientational order with periodic spacing between unit cells. QCs are materials with long range translational order and long range orientational order. However, the translational order is not periodic and QCs do not have rotational point symmetry [2]. A model of quasiperiodic tiling can be applied to QCs. A repeating motif fills space with unit cells or "tiles" in a way that maintains long range order without periodicity, a famous example is the Penrose tiling [3]. Surface science studies so far have tried to combine intermetallic QCs with common materials either by depositing single elemental adlayers on QC surfaces or by thin-film deposition of QC materials onto periodic lattices. In 2013 Stefan Foster investigated a method of forming a two dimensional QC phase for the growth of $BaTiO_3$ with preferential pseudocubic structure of an elemental metal substrate with 3 fold symmetry. The experiment found that an aperiodic QC structure can be formed by annealing a $BaTiO_3(111)$ layer several monolayers thick on a Pt(111) substrate. On being annealed to 1,250K in a ultra high vacuum (UHV), the film restructures into a QC thin film. $BaTiO_3$ is a thoroughly investigated perovskite oxide and is also widely used in thin film applications and oxide heterostructures. In its paraelectric phase it crystallizes into a simple cubic lattice. As a result of matching lattice conditions it can be grown on many other perovskite substrates and also on metal substrates [4]. This project will attempt to prepare a Pt(111) surface in the context of the Stefan Foster experiment. The Pt(111) surface will be examined using scanning tunneling microscoscopy (STM) and low energy electron diffraction (LEED)

In a solid, atoms are packed together by a coulomb forces. Physical properties of solids are governed by the nature of bonds and arrangement of atoms. A surface is formed by breaking bonds, i.e. surface atoms have less neighbouring atoms than bulk atoms. Dangling bonds at the surface causes a state of elevated energy. Surface atoms also enhance chemical activity. In order to compensate for the loss of bonding, surface atoms may rearrange and develop a new equilibrium position. Thus, the surface structure and physical properties are expected to be different from the bulk properties. There are two possibilties of arrangement of atoms: atoms may arrange within the surface (surface reconstruction) or whole atoms in the surface plane may relax vertically (surface relaxation). Early investigations of QCs were motivated mainly by whether or not properties such as surface reconstruction or surface relaxation are relevant to this class of materials [5]. Surface science studies are important to understand the proper-

ties of QCs. Quasicrystalline alloys have high hardness, low surface energy, and nonstick properties comparable to Teflon. QCs are too brittle to be used in bulk form in many applications but they may prove useful as surface coatings or functionalising thin films, for example QC coatings may be used in contact mechanical applications or for reducing adhesion because QC coatings often offers poor bonding to contact materials due to their low surface friction. QCs may also be used as heat insulators, at room temperature an Al-Cu-Fe QC has a heat conductivity value of $1WmK^{-1}$ this property of QCs could be used in aircraft turbine blades to increase engine efficiency and prolong the use of the turbine blades [6].

2 Quasicrystal and Surface Physics Overview

Surface physics is the study of atomic arrangements and chemical composition at surfaces and interfaces of a solid. It involves creating theoretical frameworks and making observations of the mechanical, electronic and chemical properties of surface interfaces. A solid interface is defined as a small number of atomic layers that separate two solids in contact with one another, where the properties differ significantly from those of the bulk material it separates [7]. Traditionally solids have been sub-classified as crystal and amorphous structures [2]. Amporphous materials were seen as disordered materials whereas crystalline phases were seen as the best representation of periodic order [8]. The discovery of QCs has opened a new area of research in the field of condensed matter physics. The QC is a form of solid that differs from the amorphous and crystal states. QCs are intermetallic compounds possessing long-range order with a lack of periodicity and often exhibit rotational symmetries which are forbidden in the conventional model of crystals. Early studies were motivated by whether surface structural phenomena such as step-terrace formation is present in QCs [5]. QC surface research have technological applications in surface coatings and solutions to kink deformations in composite materials and electronics.

2.1 Tiling

Tilings are a family of mathematical sets comprising of tiles that cover a plane without gaps or overlaps [9]. Tiling methods are not explicitly used in this report but they are worth discussing due to their use in the modelling of QC structures. A "set" is a collection of distinct objects, for example {1,2,3} is a set but {5,1,5} is not because 5 appears twice. The distinct objects are referred to as "tiles". Instead of a set of numbers, we can use a set of shapes [10]. This is the foundation of QC tiling, though a special consideration for the aperiodic translational order found in QCs is required.

2.1.1 The Fibonacci Sequence for 1D Tiling

The Fibonacci sequence is an example of a 1D quasiperiodic substitutional sequence. It follows the substitution rules $\sigma : L \longmapsto LS, S \longmapsto L$. The matrix representation of the Fibonacci sequence is

$$\sigma : \begin{pmatrix} L \\ S \end{pmatrix} \longmapsto \begin{pmatrix} 1 & 1 \\ 1 & 0 \end{pmatrix} \begin{pmatrix} L \\ S \end{pmatrix} = \begin{pmatrix} LS \\ L \end{pmatrix} \tag{1}$$

This matrix does not yet produce a quasiperiodic pattern, it merely calculates the relative frequencies of n steps of the generated words w_n; which are finite strings of the possible frequencies of the letters {L,S}. A sequence which yields a quasiperiodic pattern of $w_n = \sigma^n(L)$ for the n^{th} iteration of $\sigma(L) : L \longmapsto LS$ is created by the recursive concatenation of shorter words according to the concatenation rule $w_{n+2} = w_{n+1}w_n$ [11]. The number of letters inflates ad infinitum without repetitions of the ordering of the letters, hence a quasiperiodic pattern which can be used as a method of tiling.

2.1.2 Penrose Tiling

The Penrose pattern is comprised of a finite number of rhombi with matching rules which constrain the way neighbouring tiles can join together edge-to-edge [12]. The "matching rules" are known as the adjacency rules. Figure 1 shows two sets of tiles which can be used in Penrose tiling, both have the same adjacency rule. The vertices of individual tiles are assigned colours. The vertices must be joined such that in infinite tiling each vertex is a single colour [13].

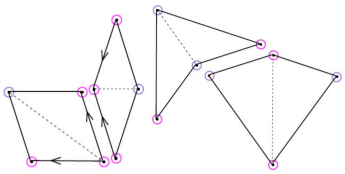

Figure 1: Left: adjacency rules for rhombs method. Right: adjacency rules for kite and dart method. Reprinted from [13]

Since the discovery of QCs a significant line of research has been dedicated to developing explanations as to why atoms restructure into complex quasi-periodic structures rather than simple crystal structures [14]. One explanation is that atoms form discrete clusters much like the Penrose tiles shown in Figure 1. However, this explanation is criticized because the adjacency rules required to form a quasi-periodic pattern in the Penrose tile model are complicated but in 1996 Steinhardt et al showed that a QC tiling could be produced with just a single tiling [15].

2.1.3 Dodecaganol Tiling

Decagonal phase quasicrystals with 12-fold symmetry were first reported by T. Ishimasa et al in 1984 [16]. Figure 2 shows the dodecagonal tiling construction used in the Stefan Foster experiment [4]. The tiling is constructed from squares and triangles which enclose angles of 90° and 60°, respectively, and can assume twelve orientations at 30° intervals [17]. The edge lengths represent the bond lengths of the atoms, which are equivalent to the lattice constant (i.e. unit length). Building up this lattice leads to increasing generations of dodecagons where the centre of each dodecagon lies at the corner of a $2 + \sqrt{3}$ scale larger dodecagonal structure

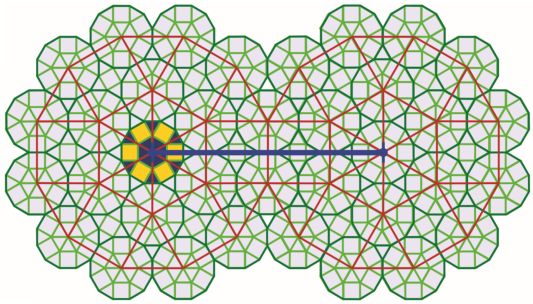

Figure 2: An ideal dodecagonal 12-fold tiling arrangement built up from equilateral triangles and squares. Reprinted from [4]

2.2 Some Nomenclature

The surfaces of crystals consists of flat planes known as terraces. The surface of crystals also contains steps, the height of the steps are constrained by the inter-planar spacing of the material. An adatom is an atom which exists on the surface of the crystal with no near neighbour atoms lying on the same plane, if a collection of atoms neighbour one another but not in significant number, it is referred to as an island. A vacancy is a defect in which an atom is missing from the surface structure [18][19].

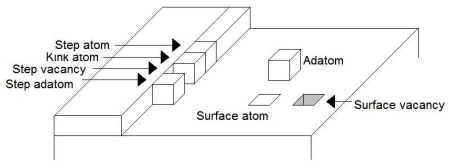

Figure 3: Illustration showing some exaples of surface science definitions. Reprinted from: [20]

2.3 Surface Reconstruction and Relaxation

Surface reconstruction and relaxation are phenomena which generally arise from differences in coordination of the bulk and surface atoms. These differences influence the distribution of electrons surrounding the atoms. As a result, the equilibrium structure of the surface plane may be different from the equilibrium structure of the bulk lattice planes [21]. Surface atoms do not retain bulk properties. The atoms near and at the surface of the bulk structure become displaced from the ideal bulk positions. The surface atoms rearrange themselves to form new ideal equilibrium positions as a result of differences of the atomic and electronic environment between the surface and bulk positions. Surface relaxation refers to the rearrangement of the surface plane. It involves variation in the plane spacings perpendicular to the surface plane and there is no change in periodicity parallel to the surface, or symmetry of the surface. Surface reconstruction refers to significant displacements of surface atoms that change the periodicity of the surface [22].

2.4 Surface Crystallography

The lattice of an adsorbed phase with a unit cell larger than the surface cell is called a superlatice, the associated structure a superstructure. Adsorbate superstructures frequently go along with a reconstruction of the substrate. Base vectors of the until cell of superstructures and surface reconstructions are expressed in terms of the base vectors of the unit cell of the truncated bulk. With s_1 and s_2 as vectors spanning the surface unit cell of a truncated bulk lattice, the lattice vectors of the actual unit cell on the surface, a_1 and a_2 are described by the matrix $\mathbf{t}$.

$$\begin{bmatrix} a_1 \\ a_2 \end{bmatrix} = \begin{bmatrix} t_{11} & t_{12} \\ t_{21} & t_{22} \end{bmatrix} \begin{bmatrix} s_1 \\ s_2 \end{bmatrix} \tag{2}$$

With,

$$a_1 = t_{11}s_1 + t_{12}s_1 \tag{3}$$

$$a_2 = t_{21}s_1 + t_{22}s_2 \tag{4}$$

Another method for specifying the relationship between the subtstrate and the lattice is Wood's notation. The substrate lattice and superlattice can be desribed by,

$$r_{sub} = n_1a_1 + n_2a_2 \tag{5}$$

$$r_{sup} = n_1b_1 + n_2b_2 \tag{6}$$

Where a_1,a_2 are the unit vectors of the substrate and b_1,b_2 are the unit vectors of the superlattice. Wood's notation is applicable only if the angle between b_1,b_2 is the same as that between a_1,a_2.

2.5 Electronic Structure of Surfaces

Modelling the electronic structure of surface atoms is difficult if considering a many-body Schrödinger equation since there's a vast number of electrons interacting with one another. The model can be simplified by attribution an effective one particle potential equation [23]

$$\begin{aligned} -\frac{1}{2}\nabla^2\psi_i(r) &= \left(\sum_I v_{ion}(r-r_i) + V_H(r) + V_{xi}(r)\right)\psi_i(r) \\ &= \epsilon_r\psi_i(r) \end{aligned} \tag{7}$$

V_H is the Hartree potential, it's the potential field which an electron moves through. The potential field originates from the electrons interactions with the positively charged nuclei and the charge density due to other electrons in the environment, it is given by

$$V_H = \int v(r-r^{'})\rho_0(r^{'})dr^{'} \tag{8}$$

The density of states ρ_0 is given by

$$\rho_0(r) = \sum_i |\psi_i(r)|^2 \tag{9}$$

This assumes that electrons are independent of one another. The density of states is derived from the summation of the single electron eigenstates [24] .

2.6 Epitaxial Growth

Thin film growth is when the adsorbate exceeds a thickness greater than one mono-layer. Epitaxial growth refers to orientated growth. It is referred to as homoepitaxy if the substrate and adlayer are the same material and heteroepitaxy if the substrate and adlayer are different materials. There are three main types of epitaxial growth modes. These modes are: Frank-van der Merve mode (layer-by-layer), Volmer-Weber mode (Island growth) and the Stranski-Krastanov mode (layer plus island mode). Frank-van der Merwe used elasticity theory to derive the concept of a critical misfit below which layer-by-layer growth occurs. Volmer and Weber created a model of growth based on nucleation theory whereby crystalline films grew from nuclei on the substrate and their relative number and growth rate was proportional to interfacial and surface free energies. Stranski and Krastanov considered crystal growth to begin with a few pseudomorhpic 2D layers, on top of which 3D crystals with their natural lattice constant will grow [25]. Molecular Beam Epitaxy (MBE) is a UHV based technique for producing epitaxial structures through the deposition of a vaporized beam of atoms or molecular clusters onto a surface [26]. The source materials are placed in evaporation cells which provide an angular distribution of atoms or molecular clusters in the beam [27]. The source material can be heated through the use of Knudsen cell evaporators which use a method of ohmic heating to evaporate the source material.

2.7 Quasicrystal Applications

QCs may have important applications as technological materials. QCs could be used to resolve kink deformations in composite metal alloys, increasing the mechanical strength of the material. QCs also have applications in LED technology, thermal coatings and hydrogen fuel storage. More trivial examples include non-stick coatings for cooking equipment.

2.7.1 Applications in Aerospace Industry

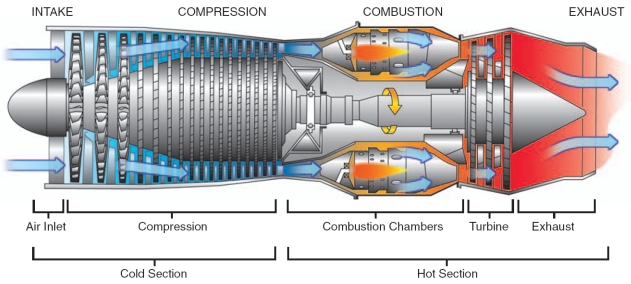

Figure 4: Diagram of a typical gas turbine jet engine. Air is compressed by the fan blades as it enters the engine, and it is mixed and burned with fuel in the combustion section. The hot exhaust gases provide forward thrust and turn the turbines which drive the compressor fan blades [28] .

In supersonic flight military jet engines, maximum thrust is sought by increasing the exit velocity of the jet engine at the expense of fuel economy [29]. At high exit velocities turbine blades must reach high rotational velocities and the blades undergo high thermal and mechanical stress. This increases the likelihood of creep deformation, which is the permanent plastic deformation of a material. Creep deformation leads to the elongation of turbine blades which may hit the engine casing and lead to engine failure. First generation turbine blades were polycrystalline, with random grain orientations and sizes. The next advance was an aligned polycrystalline structure, with a strength increase in the long axis direction of the blade. Latest generation blades are single crystal, eliminating the mechanically weak grain boundaries. The blades are usually coated in a ceramic to increase the blade's resistance to corrosion. In a secondary process known as thermal barrier coating, blades can be coated with a ceramic to increase thermal resistance of the blade to above the melting temperature of the blade [30]. Coatings on modern aero-engines are normally deposited to a ceramic layer thickness of 125-200µm which increase the operating temperature of the turbine blades on the order of 60 to 100K. The strain tolerance of thermal barrier coating systems is limited by the properties of the ceramic coating. The material properties of ceramics lead to additional complications owing to their low thermal expansion, high Young's modulus and inherent brittleness. This can result in a misfit between the ceramic coating and metallic blade substrate

since the ceramic can crack and fragment, leading to a loss of coating [31]. The low thermal conductivity and corrosion resistance found in QCs is useful for turbine blade coatings when the QC is superplastic, such as the thermally stable quasicrystal Mg-Zn-Y-Zr [32]. Quasicrystals can accommodate the high thermal and mechanical stress present in an operating jet engine.

2.7.2 Applications in Hydrogen Fuel Storage

Hydrogen forms metal hydrides with some metals and alloys leading to solid-state storage under moderate temperature and pressure that gives them an important safety advantage over the gas and liquid hydrogen storage methods [33]. TiFe hydrides have successfully been used as storage tanks for hydrogen internal-combustion engines but they tend to form stable hydrides which prevents the ready desorption of the stored hydrogen for the intended use [34]. Ti-Zr quasicrystals have greater capacity for reversible hydrogen storage and are less likely to hydrogenate. Hydrogenation would lead to an irreversible formation of a crystalline hydride phase [35].

3 Experimental Techniques

The effects of ambient gases on materials at an atomic scale are much more pronounced. The main focus of experimental techniques used in surface science studies is to increase the mean free path of molecules within the system of experiment, this decreases the effect that ambient molecules within the system of experiment have on the surface which is under investigation. Surface science experiments make use of ultra high vacuums (UHV) systems on the scale of 10^{-8}mbar or less [36]. UHV systems require a special build which takes into account outgassing, operating temperatures and differential pressures acting on the build. All of which have the purpose of increasing the mean free path of molecules in the system and to avoid contamination of the surfaces under investigation.

3.1 Ultra High Vacuum Technology

Surface science experiments require a UHV to avoid contamination of the surface from ambient gases, a UHV keeps the surface of the samples clean over the period of the experiment. Contaminants can interfere with measurments due to the presence of electrons, ions and atoms within ambient gases. Outgassing is a significant source of ambient gases within the UHV system. Outgassing refers to the liberation of gases and vapors from the walls of a vacuum chamber or other components on the inside of a vacuum system [37]. The mechanisms behind outgassing include thermal desorption, desorption induced by electronic transitions, vaporisation of materials, gas diffusion from the bulk and subsequent desorption and permeation through the UHV chamber walls [38]. Gases can

permeate through most materials, this means that ambient gases in the atmosphere can permeate through the UHV chamber walls into the vacuum system. Atmospheric gases dissolve into the UHV chamber walls which then diffuse into the the inner wall of the system, when the gases arrive to the inner walls of the UHV chamber they desorb into the UHV system. The dissolution is described by Henry's law:

$$c = sP \tag{10}$$

c is the concentration, P is the gas pressure, s the solubility. The diffusion process is described by Fick's 1st law

$$Q = -D\frac{dc}{dx} \tag{11}$$

Q is the total gas flow and D is the diffusion coefficient. It is important to note that the diffusion coefficient D, depends exponentially on temperature [39]

$$D = D_0 e^{-\frac{E}{kT}} \tag{12}$$

Where E is the binding energy of the gas molecule. It is necessary to heat up a vacuum chamber to remove the adsorbed gas, this is known as a bake out. The UHV system is typically heated to 350°C and maintained for a period of time, usually 24 hours. The temperature and time of the bake out depend of the characteristics of the material build of the UHV system and the diffusing gas. The bake out temperature must be high enough to to overcome the binding energies of the adsorbed atoms [40].

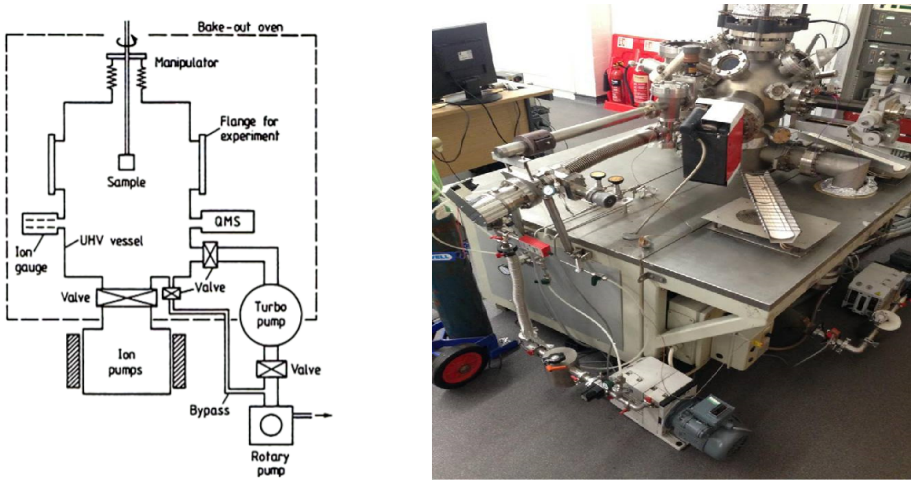

Figure 5: (a) Schematic showing the typical construction of a UHV system. (b) Image of UHV used in this experiment, courtesy of Dominic Burnie.

Reducing the effect of outgassing is an important factor in the reduction of surface contamination in a UHV experiment. The rate of surface contamination depends on the flux of gas molecules (Z) and the sticking coefficient (S). The flux is defined as the number of gas molecules colliding the unit area of the surface per second and is derived from the kinetic theory of gases. The Maxwell-Boltzmann velocity distribution is given by

$$\frac{dn}{dv} = \frac{2N}{\pi^{\frac{1}{2}}}\left(\frac{m}{2kT}\right)^{\frac{3}{2}} v^2 e^{-\frac{mv^2}{2kT}} \tag{13}$$

Where N is the total number of molecules, m is the mass of each paticle, k is the Boltzmann constant, T is the average temperature of the molecules and v is the average velocity of the molecules. The average particle velocity is given by

$$\overline{v} = \left(\frac{8KT}{\pi m}\right)^{\frac{1}{2}} \tag{14}$$

A molecule that moves with speed v and covers an area σ covers a volume $V = \sigma d = \sigma v t$ in a time t. In reality, the molecule will have N collisions with other molecules and will have a random, chaotic motion. It is required that we consider the average velocity of molecules within the system, $\overline{v}$. The mean collision time is given by $\tau = \frac{t}{N}$. For a large volume of gas

$$\tau = \frac{t}{N} = \frac{t}{nV} = \frac{t}{n\sigma\overline{v}t} = \frac{1}{n\sigma\overline{v}} \tag{15}$$

Another $\overline{v}$ term must be added to correct for the average distance travelled per molecules and a factor of $\sqrt{2}$ is added to account for the uncorrelated motion of individual particles [41] [42].

$$\lambda = \frac{1}{\sqrt{2}n\sigma} \tag{16}$$

This is the average distance that a particle travels in the gas phase between collisions, for a simple hard-sphere collision model,

$$\lambda = \frac{1}{\sqrt{2}n\pi d^2} \tag{17}$$

The sticking coefficient is defined as the fraction of incident molecules which adsorb upon the surface. The sticking coefficient depends on various parameters such as temperature and surface structure. S is low at high temperatures and high at low temperatures.

3.1.1 UHV Chambers

UHV chambers require a special construction. The materials used in the build should have a low outgassing rate, an ability to operate at high temperatures during bake outs and due to the differential pressures acting on the system, the

materials used should be robust enough to maintain their ambient form during their operation in UHV experiments. Stainless steel makes a great compromise between these properties. It has an extremely low outgassing rate of $Q = 2 \times 10^{-14}\text{TorrL}s^{-1}cm^{-2}$ [43] with a melting point between the range of 1400 to 1450°C [44] Stainless steel flanges are used in UHV systems for sealing the chamber. The vacuum joints are made with metal seals such as gold wire o-rings. The vacuum chamber and associated pipework such as the pipes used for sputtering (which will be discussed later in the report) are made from stainless steel.

3.1.2 Vacuum Pumps

The turbomolecular pump was developed and patented at Pfeiffer Vacuum in 1958 by Dr. W Becker. The turbomolecular pump is a type of kinetic vacuum pump. The design of the turbomolecular pump can be likened to a turbine. It's a multi-stage, turbine-like rotor with bladed disks which rotate in a casing. The turbomolecular pump consists of rotor and stator pairs with angled blades inclined in reverse directions, mounted in series. These blade operate at rotational velocities between 15,000 and 30,000 rpm. The pumping effect is based upon the transfer of impulse from the rapidly rotating blades to the gas molecules being pumped. Molecules that collide with the blade are adsorbed there and leave the blades again after a certain period of time. In this process the blade speed is added to the thermal molecular speed [45]. The rotor blades of the pump hit the gas molecules which are transferred to the next rotor stage, directed by the stator. The momentum of the rotor transfers to gas molecules which are coming from an inlet. The molecules are finally removed by a roughening pump (usually a rotary pump) [46].

The rotary pump uses a rotating element which "impels" the energy of a fluid. A collector (volute or diffusor) guides the fluid to discharge. The rotor has a variable length, spring tensioned vane. The vane is pressed against the wall of the chamber when the rotor is driven to rotate. the pump has an inlet to the vacuum system and an outlet to the atmosphere. During the inlet phase, the volume near the inlet expands. After further rotation, the gas molecules are separated from the inlet. Further rotation of the rotor causes compression of this volume and a valve is opened which allows gas molecules to be swept through the outlet [47].

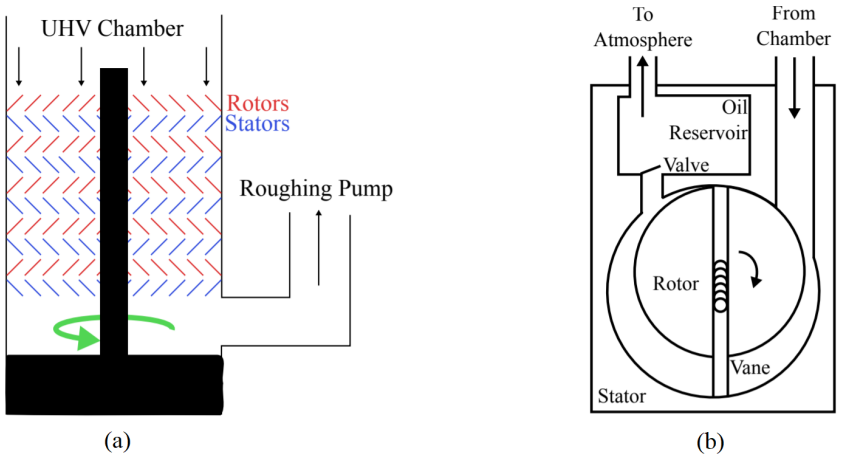

Figure 6: (a) shows a cross-section of the turbomolecular pump. The rotor and stator pairs are angled blades inclined in reverse directions, mounted in series. These blades operate at rotational velocities between 15,000 and 30,000 rpm. The pumping effect is based upon the transfer of impulse from the rapidly rotating blades to the gas molecules being pumped. The rotor blades of the pump hit the gas molecules which are transferred to the next rotor stage, directed by the stator (b) shows a schematic of a rotary vane pump. The vane is driven to rotate and the volume near the inlet expands, after further rotation the gas molecules are separated from the inlet. Further rotation causes compression of this volume and a valve is opened which allows gas molecules to swept through the outlet. Reprinted from [48].

3.1.3 Pressure Gauges

The Pirani guage is a type of thermal-conductivity vacuum sensor. Ever since its conception in 1906, the Pirani guage has been a widely used vacuum gauge for measuring pressures within the regions of 10^{-4} to 100 Torr [49]. The pirani gauge is based on the principle that the heat loss of an hot object to the ambient depends on the pressure of the surrounding gas. Therefore, the vacuum pressure can be calculated according to the heat loss variation which manifests itself by a temperature change on a thermally sensitive physical parameter associated with a hot object [50]. In practice, a typical pirani gauge consists of a filament wire in a metal or glass tube attached to a vacuum chamber. The wire loses heat by collision of gas molecules present in the chamber. The temperature variations of the filament with pressure are measured in terms of the change of resistance in the filament wire. The resistivity is usually measured using a Wheatstone bridge, in which one leg of the bridge is the filament of the gauge.

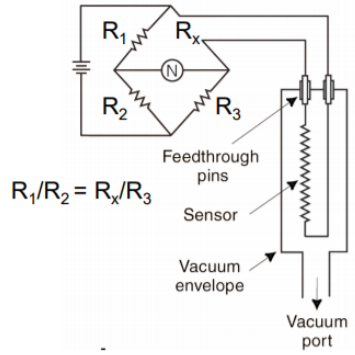

Figure 7: Schematic of a Pirani gauge, showing the Wheatstone bridge configuration. Gas molecules collide with the sensor, which causes a loss of heat in the sensor. The resistivity of the system is measured using the Wheatstone bridge.

Another type of pressure gauge is the Ionization gauge. Ionization gauges work on the principle that thermally emitted electrons from a cathode which are accelerated by an anode potential, ionize gas molecules on their path to the anode. The ion current is measured by a collector which is related to the ambient pressure. For a constant value of accelerating voltage, the number of positive ions formed per electron varies linearly with pressure. Consequently, a determination of the rate of production of positive ions for a given electron current yields a measure of pressure. The sensitivity of the gauge, defined by S can be related to the positive ion and electron currents i_p and i_e at a given pressure P.

$$S = \frac{i_p}{P i_e} \tag{18}$$

$$P = \frac{1}{S}\frac{i_p}{i_e} \tag{19}$$

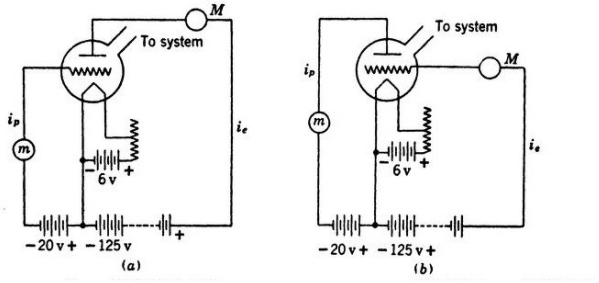

Figure 8: Electrical circuits for the ionization gauge. (a) Internal-control type. (b) External-control type.

The gauge consists of three electrodes sealed in a glass bulb which serve as cathode, anode and collector of positive ions. The collector is situated between the electrodes. The internal-control type is a type of construction in which the middle electrode functions as a positive ion collector. The external-control type is a type of construction in which the outer electrode functions as a positive ion collector [51].

3.2 Low Energy Electron Diffraction

Low Energy Electron Diffraction (LEED) gives information on symmetry and geometric arrangement of atoms near the surface of the target substrate. A collimated beam of electrons of well defined low energy (typically 20-500eV) which originates from an electron gun by an accelerating voltage are incident on a sample. The intensity of the electron beam decays exponentially with the penetration depth, d.

$$I(d_{eff}) = I_0 e^{\frac{-d_{eff}}{\mu}} = I_0 e^{\frac{-d}{\mu \cos\theta}} \tag{20}$$

where I_0 is the initial beam intensity, θ is the angle of beam incidence and μ is the inelastic mean free path of electrons (attenuation length). The diffracted electrons pass through a series of grids before colliding with a flourescent coating on a screen, where light is emitted. The first and last grids are held at the ground potential to confine the field. The central grids are kept close to V, such that only elastically scattered electrons are selected. A view port is present behind the screen where the LEED pattern can be observed by eye or can be recorded with a camera.

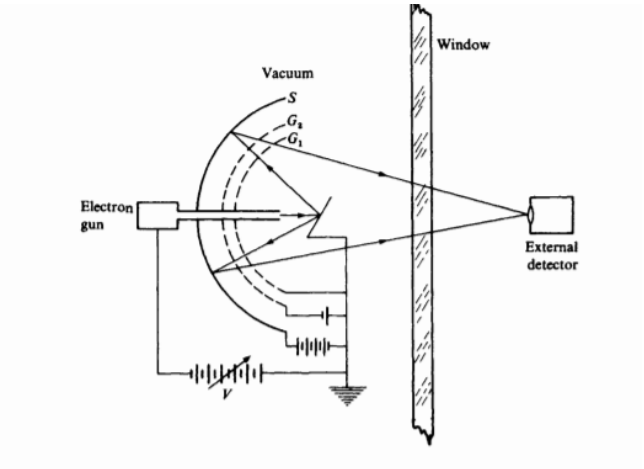

Figure 9: Schematic display-type LEED system.

The displayed diffracted beams are referred to as LEED spots. The brightness of the LEED spots are proportional to the intensities of the corresponding

diffracted beams [52]. The de Broglie wavelength of the incident electrons λ_i is given by,

$$\lambda_i(\mathring{A}) = \frac{h}{\sqrt{2E_k m}} \tag{21}$$

The scattering of electrons by a single atom is described by the atomic structure factor: $f_n(K, k_i)$. Where $K = k_i - k_f$ is the scattering vector. The structure factor of the whole sample is obtained from the summation of all of the scattered waves functions, thus the sum over all the atomic positions at position r_n,

$$\psi(K, k_i) = \sum_n f_n(K, k_i) e^{iKr_n} \tag{22}$$

The diffracted intensity is given by,

$$\begin{aligned} I(K, k_i) =& \mid \psi(K, k_i) \mid^2 = \psi(K, k_i)\psi^*(K, k_i) \\ &= \sum_{n,m} f_n(K, K_i) f_m^*(K, k_i) e^{iK(r_n - r_m)} \end{aligned} \tag{23}$$

In the kinematic approximation electrons undergo single scattering and structure factors are identical for atoms of the same elements, therefore,

$$\begin{aligned} I(K, k_i) &= \mid f(K, k_i) \mid^2 \sum_{n,m} e^{iK(r_n - r_m)} \\ &= \mid f(K, k_i) \mid^2 g(K) \end{aligned} \tag{24}$$

Where $g(K)$ is called the lattice factor:

$$g(K) = \sum_{n,m} e^{iK(r_n - r_m)} \tag{25}$$

The conditions under which diffraction can be observed are described by three Laue-equations, which can be expressed in terms of a single vector equation

$$k = k_0 = G \tag{26}$$

in which k and k_0 are the wave vectors of the scattered and incident wave and G is an abritray vector of the reciprocal space. At the surface of the sample, the bulk periodicity is truncated and the three Laue-equations reduces to,

$$k_\parallel = k_{0\parallel} = G_\parallel \tag{27}$$

The Laue condition is illustrated with the Ewald-construction in Figure 9. The Ewald sphere is constructed by drawing the reciprocal lattice rods normal to the surface, which are seperated by $\frac{2\pi}{a}$, a being the interatomic spacing. The wavevector of the incident beam k_0 is positioned with its end at the point $(0, 0)$ of the reciprocal lattice rod. A sphere is then drawn from point $(0, 0)$ of k_0. The diffraction condition is fulfilled at the point of intersection of the sphere and rod

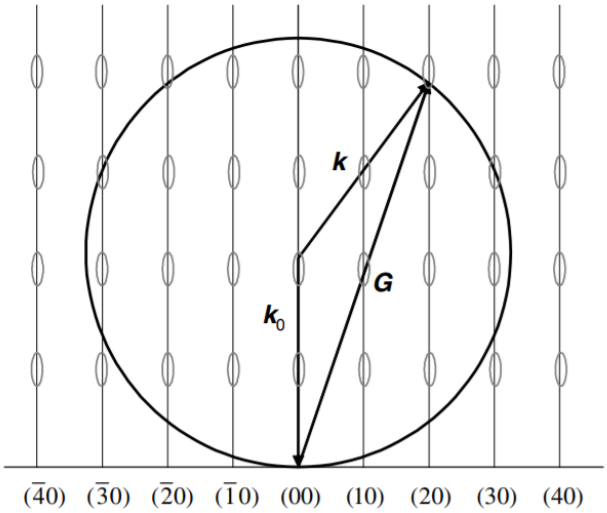

Figure 10: Ewald-construction for surface scattering in a LEED experiment.

[53]. It is possible to calculate the emission angle ϑ_{hk} for a beam corresponding to the surface reciprocal lattice vector,

$$k_{\parallel} = k_{0\parallel} = G_{\parallel} = hb_1 + kb_2 \tag{28}$$

The position of the diffraction maxima is given by:

$$\begin{aligned} d_{hk} &= Rsin\vartheta_{hk} = \frac{R}{|k_f|}|hb_1 + kb_2| \\ &= R\frac{\hbar}{\sqrt{2m_e}}\frac{1}{\sqrt{E}}|hb_1 + kb_2| \end{aligned} \tag{29}$$

3.2.1 Bragg Diffraction Condition

The condition for constructive interference is given by

$$asin\theta_i = n\lambda_i \tag{30}$$

Where λ_i is the de Broglie wave of the incident electrons given by equation (21) and n is an integer. For a given value of λ_i and a, θ_i is allowed to have discrete values. The magnitude of the wavevector of incident electrons is given by

$$k = \frac{2\pi}{\lambda_i} \tag{31}$$

Applying this to the Bragg condition we get

$$ksin\theta_i = \frac{2\pi}{a}n \tag{32}$$

3.2.2 Conclusion

The existence of a sharp spot pattern produced in LEED experiments implies the existence of a well-ordered surface and provides information about the symmetry of the substrate. LEED allows for the experimentally derived information of structual quality, surface unit cell and surface morphology. The size and symmetry of the surface unit cell in real space can be determined from the positions of the diffraction spots. The variation in diffracted intensity across the width of a single spot (known as spot profiling) can be used to gain information on the surface morphology. A deviation from perfect two dimensional periodicity will cause defects in the character of the reciprocal lattice rods. The optical sharpness of spots measures the long range order of the surface [54].

3.3 Scanning Tunneling Microscope

The scanning tunneling microscope (STM) was invented by Binning and Roher 1982. It was the first successful tunneling experiment with an externally and reproducibly adjustable vacuum gap. [55]. An STM has 5 basic components: an atomically sharp conductive tip, a piezoelectric scanner, a current amplifier, a bipotentiostat (bias) and a feedback loop. The central aspect of the STM setup is a sharp conductive tip, which is moved in a very precise and controlled manner in three dimensions across the surface of the sample. A small voltage is applied between the tip and sample which is typically a few mV to a few V. A tunnelling current flows if the tip is brought close enough to the sample. The distance between the tip and sample substrate is usually between 5-10 Å, it varies according to the properties of the material under investigation.

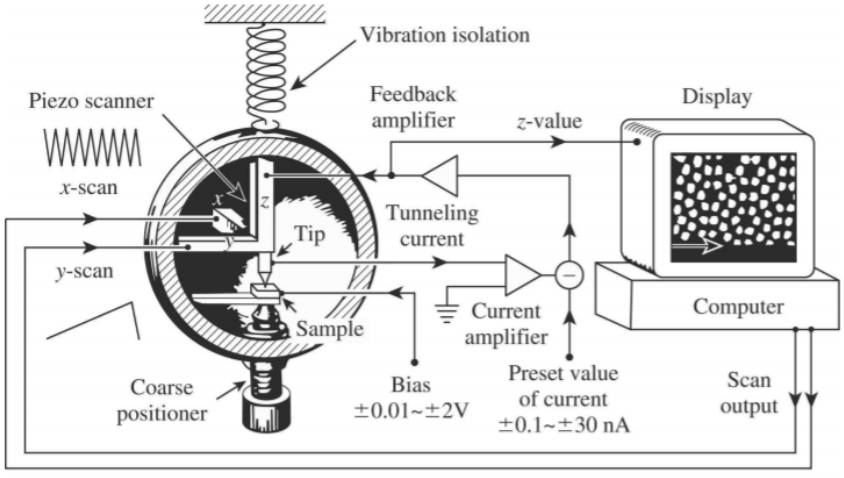

Figure 11: A schematic of an STM setup [56]

In the STM, quantum mechanical tunneling takes place between the tip and

the sample. The process can be represented as a potential well problem. Classically, an electron cannot penetrate into or across a potential barrier if its energy is less than that of the potential of the barrier. A complete and quantifiable description of the tunneling process requires a solution to the three dimensional form of the Schrödinger equation. The three dimensional Schrödinger equation has the general form:

$$H\Psi = E\Psi \tag{33}$$

Where H is the hamiltonian operator and E is the total energy operator which are expressed as

$$\frac{-\hbar^2}{2m}\nabla^2\Psi(r,t) + U\Psi(r,t) = i\hbar\frac{\partial\Psi(r,t)}{\partial t} \tag{34}$$

In a rudimentary model of STM, we can simplify the setup to a one-dimensional potential barrier and make a one-dimensional analysis of the Schrödinger equation.

$$\frac{-\hbar^2}{2m}\nabla^2\Psi(x,t) + U(x)\Psi(x,t) = i\hbar\frac{\partial\Psi(x,t)}{\partial t} \tag{35}$$

The wave function has a general solution given by

$$\Psi(x,t) = Ae^{-i(kx+\omega t)} + Be^{i(kx-\omega t)} \tag{36}$$

This is the plane wave representation for an electron wavefunction of wavenumber $k = \frac{2\pi}{\lambda}$ and angular frequency ω.

$$U(x) = \begin{cases} -U_0, & \text{for } -a \leq x \leq a \\ 0, & \text{for } |x| > a \end{cases} \tag{37}$$

The Probability of finding an electron outside the boundaries of the barrier $|x| > a$ between the substrate with width x and the probing tip is given by

$$P(x) = |\Psi(x)|^2 = |\Psi(0)|^2 e^{-2\kappa x} \tag{38}$$

A small bias voltage, V, is applied so that the tunnelling electrons which have an electric field, E, give off a tunnelling current, I. The height of the barrier can be approximated by the average workfunction of the sample tip, given by

$$\Phi = \frac{\Phi_{substrate} + \Phi_{tip}}{2} \tag{39}$$

The tunnelling current is proportional to the probability of the electrons to pass the barrier [57]

$$I \propto \sum_{E_n = E_F - eV}^{E_F} |\Psi_n(0)|^2 e^{-2\kappa d} \tag{40}$$

The tunnelling electron current is measured by scanning an atomically sharp tip across the surface of the material under examination. The tunnelling currents depends exponentially on the tip to surface separation distance [58]. In constant

current mode, a feedback network changes the height of the tip (sample to tip distance) such that the current remains constant. The height of the tip is measured using the voltage applied to the piezoelectric drive, which can be used to create a topographical map of the sample surface. In constant height mode, the distance between the sample and the probe tip is kept constant, the voltage applied to the piezoelectric drive is also kept constant. The current is monitored and the feedback network responds rapidly enough to keep the average current constant [59].

4 Surface Preperation

The UHV environment decreases the probability of surface contamination during measurement taking but there may already be contaminants which exist on the surface of the sample. The surface of the sample must first be cleaned to remove surface contaminants and the UHV environment is a necessity to maintain the clean surface over the period of the experiment.

4.1 Preliminary Sample Treatments

The surface is polished with a diamond paste before placing the sample into the UHV system. The surface morphology of the sample is influenced by the polishing method. A study by Z. Papadopolos found that 0.25μm diamond paste yields the best surface for STM studies [60].

4.2 Ion Sputtering

Ion Sputtering is the ejection of atoms by bombardment of a solid or liquid by energetic ions. The target atoms are ejected via the incident energetic ions and resultant recoil atoms with surface atoms. The removal rate of surface atoms is known as the sputter yield, Y, and is defined as the ratio between the number of sputter ejected atoms and the number of incident ions [61]. In 1984 J. Bohdansky derived a general expression for the sputter yield [62] by making assumptions for the momentum distributions of the recoil target atoms and emission ions. The general expression is given by

$$Y(E) \approx \alpha S_n(E) \left[1 - \left(\frac{E_{th}}{E}\right)^{\frac{2}{3}}\right] \left[1 - \frac{E_{th}}{E}\right]^2 \tag{41}$$

Where α is the energy-independent function of the mass ratio between the target and projectile, $S_n(E)$ is the nuclear stopping cross section, E_{th} is the energy of the ejected particles and E is the energy of the incident ions.

4.3 Annealing

Annealing is a form of heat treatment that involves a process of heating and cooling the sample. The sample is heated to a predefined temperature and then

cooled back to its ambiemt temperature. The process of annealing alters the mechanical and physical properties of the material. It allows the atoms of the surface to restructure to their equilibrium states, thus creating a smoother surface which is essential for STM imaging. Additionally, annealing is a method of removing adsorbed gases from the sample [63]. The sample is heated using the method of ohmic heating. Ohmic heating is based on the well studied dissipation of electrical energy into heat, which results in internal energy generation prortional to the square of the electric field strength and conductivity [64]. The expressions for electrical field or voltage can be derived by combining Ohm's law and the continuity equation for electrical current

$$\nabla \cdot (\sigma_i \nabla V) = 0 \tag{42}$$

where V is voltage and σ_i is the electrical conductivity. The internal heat transfer to the sample can determined by considering the thermal conductivity and internal energy generation of the sample:

$$\nabla \cdot (k_i \nabla T) + \mu_i = \rho_i C_{pi} \frac{\partial T}{\partial t} \tag{43}$$

where k is the thermal conductivity, μ_i is the specific internal energy generation rate, ρ is the density, C_{pi} is the specific heat capacity, T is the temperature and t represents time [65].

5 Results

A Pt(111) clean surface was prepared for QC thin film growth. A theoretical model for Pt(111) was created in the VESTA program, the (111) plane was sliced to show the origin of the hexagonal symmetry found in Pt(111) LEED diffraction patterns. A simulated diffraction pattern for Pt(111) was generated using the open source LEED-pat4 software to use as a comparison for the experimental LEED pattern. A UHV system was baked out for 48 hours at 160°C. After bake out a rough vacuum was created using a rotary pump. Turbomolecular, Titanium sublimation and Ion pumps were used to create an ultra high vacuum with pressure P = 10^{-9}mbar. Following the creation of a UHV environment, a Pt(111) surface was placed into the load lock chamber and then moved into the central UHV chamber. The Pt(111) surface was cleaned by 10 minute 3keV Ar^+ sputtering followed by 20 minutes of annealing at 650°C. STM images were taken at room temperature in constant height mode, the pumps were turned off during the scans to reduce the effects of mechanical noise. LEED diffraction patterns were recorded at energies E = 136.9eV and E = 67.3eV.

5.1 Theoretical VESTA Model for Pt(111)

A theoretical model for $Pt(111)$ was made in the VESTA program. Platinum has an FCC structure with a lattice constant of $3.9236\mathring{A}$ (no error given) at 293.15K [66]. The bond lengths between atoms at the corners of the structure

are equal to the lattice constant. The shortest interatomic spacing is given by $\frac{a}{\sqrt{2}}$ where a is the lattice constant.

$$\frac{a}{\sqrt{2}} = 2.77\mathring{A} \tag{44}$$

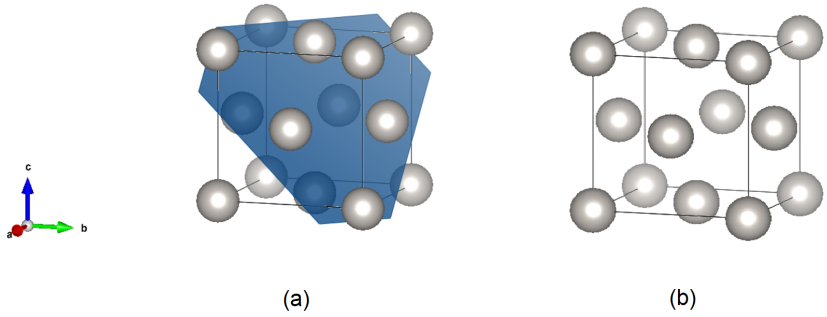

Figure 12: (a) Theoretical VESTA model for Pt(111) showing the (111) hkl plane (b) $Pt(111)$ structure without the hkl plane.

The interplanar distance is given by

$$d_{hkl} = \frac{A}{\sqrt{h^2 + k^2 + l^2}} = 2.2653x10^{-10}m \tag{45}$$

A (111) plane slice is obtained from the model, exposing the 6-fold hexagonal symmetry.

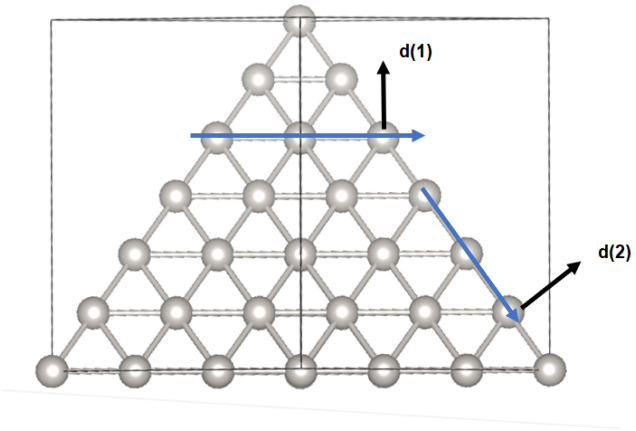

Figure 13: Slice of the Pt(111) plane from the VESTA model. The blue lines represent the possible planes which diffraction may occur.

The d(1) and d(2) diffraction planes are important for LEED analysis which is shown later in the report. The correct diffraction plane must be selected in order to calculate the true angles of Bragg diffraction.

$$d(1) = \frac{a}{\sqrt{2}} sin(60) = 2.4\mathring{A} \tag{46}$$

$$d(2) = \frac{a}{\sqrt{2}} cos(60) = 1.38\mathring{A} \tag{47}$$

The plane in which diffraction occurs is determined by the matching of the wavelength of the incident electron beam (in LEED) and the planar spacing of the surface atoms.

5.2 Interplanar Spacing for Pt(111) derived from STM Image

The interplanar spacing for Pt(111) was derived with STM images using the WSxM program [67]. The green line (known as line scan) in Fig. 12 (b) represents the range of data points used. The line scan retrieves the x-y-z coordinates for the image. The bright spots in the image were indicative of contamination. The line scan was carefully traced to avoid bright spots.

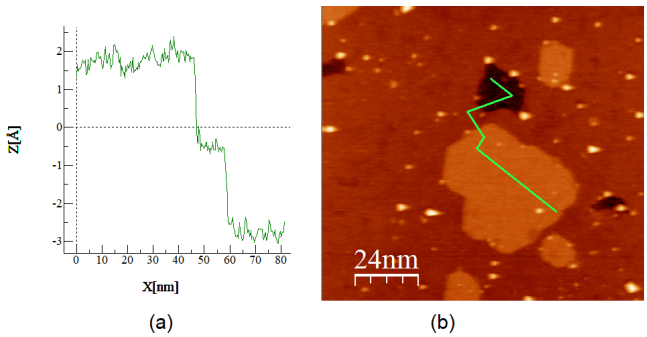

Figure 14: (a) A graph showing the terrace height distribution across the surface of the terrace (b) STM image 1 which was used to find the terrace height distribution, the green line is the line scan for height readings.

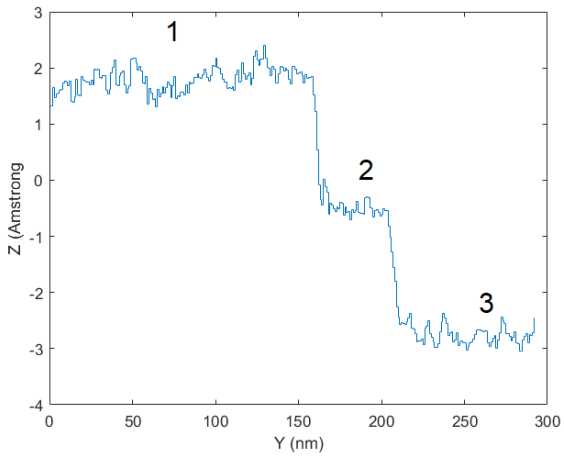

Figure 15: MATLAB plot indicating the different terrace steps labelled 1,2 and 3. The sharp peaks between the terraces are the regions of interest, they are used to determine the inter-planar spacing.

The x-y-z data points from the line scan were exported to MATLAB for examination. Fig 15 shows a plot of the Z coordinate as a function of Y. The terraces are labelled as 1, 2 and 3. Terrace 1 is where the line scan passes through the light region in Fig 14 (b). Terrace 2 is where the line scan passes through the intermediate zone between the light and dark region. Terrace 3 is where the line scan passes through the darkest region. The mean Z value for each terrace was calculated in MATLAB. The mean values were used to calculate the difference in height from terrace 1 to 2 and terrace 2 to 3. The height differences are constrained by the inter-planar spacing. The difference in height between the terraces are equal to or a multiple of the inter-planar spacing.

Terrace	d_{hkl} (Å)	Error d_{hkl} (Å)
1 to 2	2.244529	0.260397
2 to 3	2.291822	0.185275

Table 1: Table showing the experimentally determined values for the inter-planar spacing of Pt(111) from STM image 1

Another value for the inter-planar spacing for Pt(111) was found by considering the difference in height between two terraces. Figure 16 shows the STM image used.

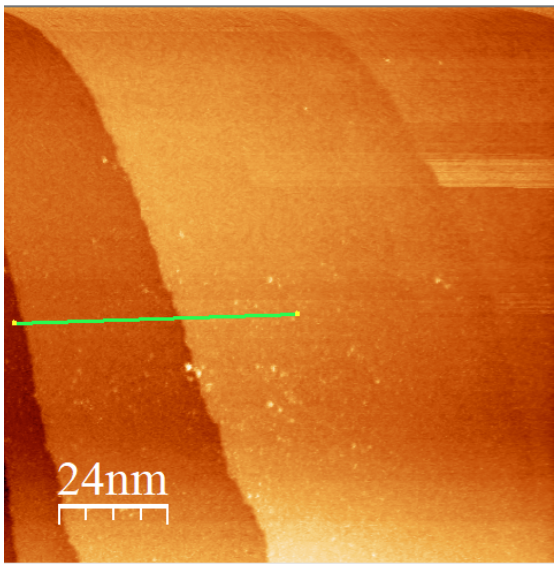

Figure 16: STM image 2 of Pt(111)

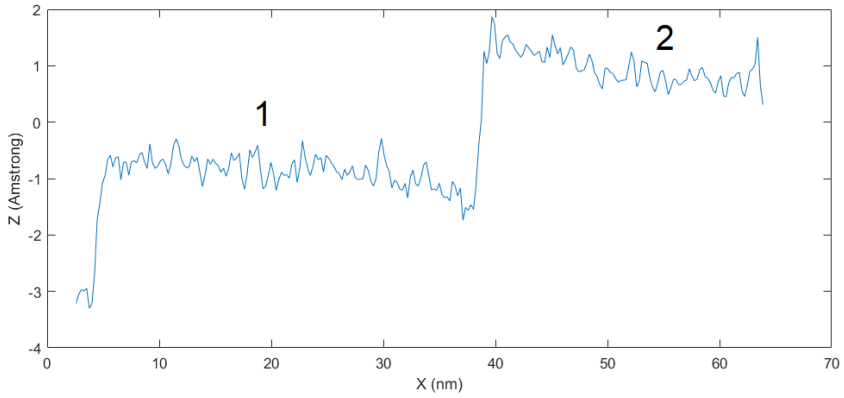

Figure 17: Terrace height Z plotted against path length X with terraces labelled as 1 and 2.

The method used for STM image 1 was also used for STM image 2. The data points from the line scan were exported to excel for examination. The mean Z value for each terrace was calculated. The difference between the Z values is equivalent to or a multiple of the inter-planar spacing. The mean Z value of terrace 1 (shown in Fig 15) was determined to be -0.9446± 0.26653 $\mathring{A}$. The mean Z value of terrace 2 (shown in Fig 15) was determined to be 0.96964 ± 0.30159 $\mathring{A}$. The difference in height between terrace 1 and 2 is 1.91419 ±

0.40249 $\mathring{A}$

5.3 LEED Results

A simulated LEED pattern for Pt(111) was created in the open source software LEED-pat4 [68]. The simulated LEED pattern shows hexagonal 6-fold symmetry with 60 degree angles between neighbouring diffraction spots.

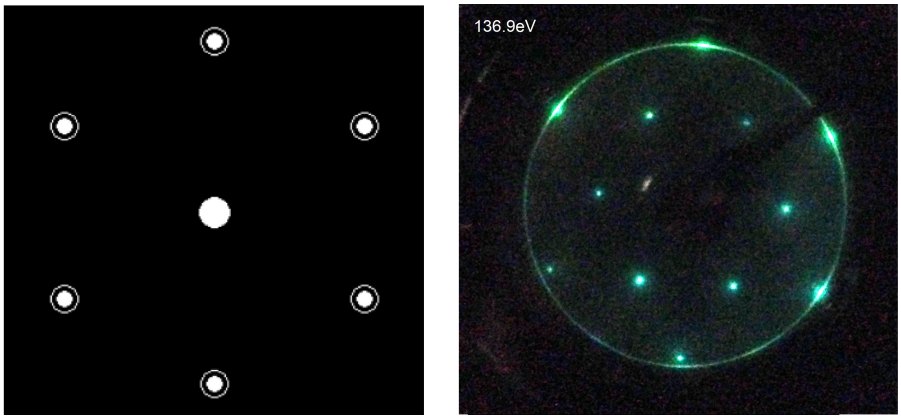

Figure 18: LHS: LEED-pat4 simulated LEED pattern for Pt(111). RHS: LEED pattern for Pt(111) at 136.9eV incident beam energy showing diffraction spots.

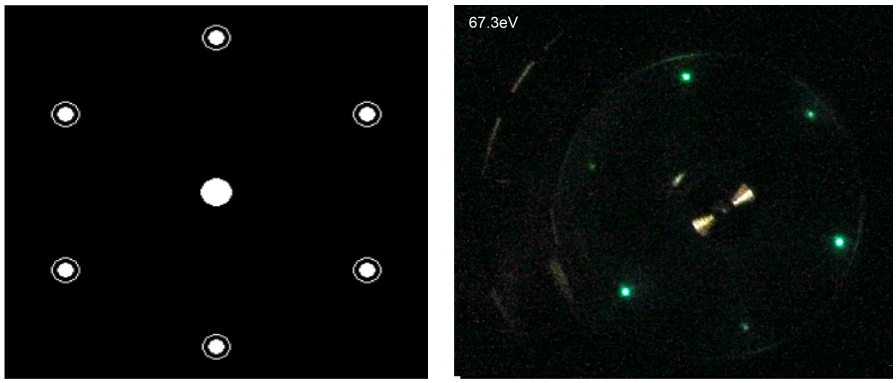

Figure 19: LHS: LEED-pat4 simulated LEED pattern for Pt(111). RHS: LEED pattern for Pt(111) at 67.3eV incident beam energy with increased contrast for clarity of diffraction spots.

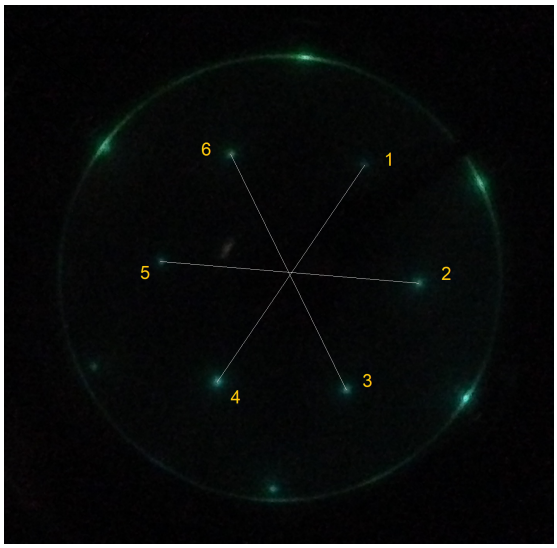

Figure 20: Pt(111) LEED pattern with 136.9eV incident beam energy. The diffraction spots are labelled. The point of intersection of the straight lines was used for measuring the radial distances of the diffraction spots.

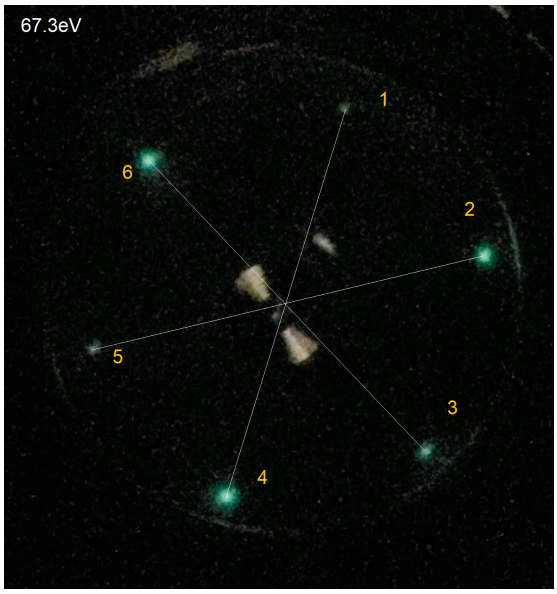

Figure 21: LEED pattern with 67.3eV incident beam energy. The diffraction spots are labelled. The point of intersection of the straight lines was used for measuring the radial distances of the diffraction spots.

The ImageJ program was used to analyze the LEED images [69]. The angles between the labelled diffraction spots were measured in the ImageJ software. The diffraction spots are diffuse, so repeated measurments were taken to reduce error. The ImageJ angle tool was used to measure the angles. The angles between the diffraction spots were measured in a clockwise manner, each angle was measure 3 times.

Diffraction Spots	Mean Angle (degrees)	Angle Error (degrees)
1 to 2	60.07	0.70
2 to 3	60.10	0.09
3 to 4	60.21	0.51
4 to 5	59.97	0.54
5 to 6	59.78	0.44

Table 2: Table showing mean angles between LEED diffraction spots with electron beam energy E = 137.6eV.

Diffraction Spots	Mean Angle (degrees)	Angle Error (degrees)
1 to 2	60.24	0.37
2 to 3	59.98	0.13
3 to 4	60.10	0.42
4 to 5	59.82	0.57
5 to 6	60.05	0.35

Table 3: Table showing mean angles between LEED diffraction spots with electron beam energy E = 67.3eV.

5.3.1 Diffraction Angles

The angle of diffraction for each diffraction spot in the LEED patterns was determined from the geometry of the experimental setup (Figure 22).

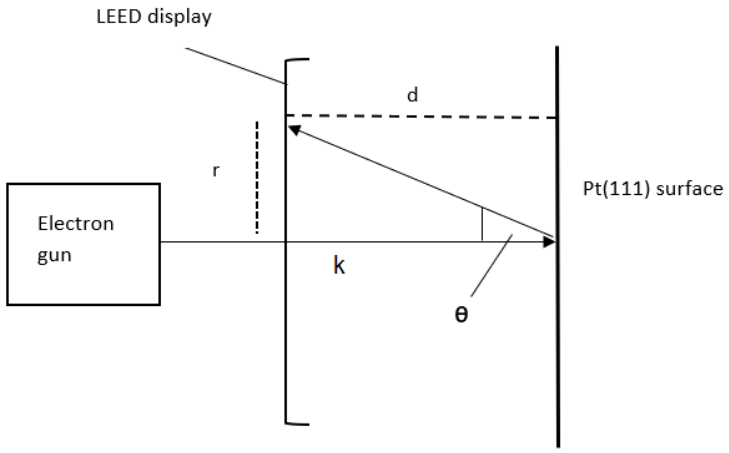

Figure 22: Diagram showing the geometry of the experimental setup

Type	Value (dimension)
Screen view angle	102 (degrees)
Spherical radius	66 (mm)
Circular diameter	104 (mm)
Electron beam current	1.2 (A)
Screen voltage	4-5kV

Table 4: Table showing specifications for Omnicron SpectraLEED, The LEED display screen used in this experiment

The specifications for the experimental setup are shown in table (4). The screen diameter of the LEED setup is 104mm. The distance from the Pt(111) surface to the LEED display is 66mm. The screen has a diameter of 104mm so the perpendicular distance from the point at which electrons are backscattered and the point at which the diffraction spot is displayed can calculated by determining the number of pixels per meter in the image. The number of pixels per meter was calculated by measuring the diameter of the display screen in units of pixels and dividing it by the diameter in meters (shown in table 4). The number of pixels per meter was determined to be 10946.154 $\pm$ 44.6 Pixelsm^{-1}. Coordinates were measured in the ImageJ program for the points of diffraction

and the point at which the diffraction spots focus on (the line intersection in fig 21 and 20). The diffraction spots are diffuse show the ImageJ multispot tool was used to create a mean coordinate of the diffraction spot. The length of the straight line between the point of focus and diffraction spot is calculated using the equation

$$\mid r \mid = \sqrt{(x_2 - x_1) + (y_2 - y_1)} \tag{48}$$

(x_2 , y_2) is the coordinate of the diffraction spot and (x_1 , y_1) is the coordinate of the intersection point. The length of the line is converted into meters by dividing the length of line by the number of pixels per meter. From figure 22 we find

$$\theta = sin^{-1}\left(\frac{r}{d}\right) \tag{49}$$

Diffraction Spot	Angle (degrees)	Angle Error (degrees)
1	27.74	0.38
2	27.42	0.33
3	27.67	0.37
4	28.02	0.42
5	27.6	0.35
6	28.05	0.34

Table 5: Table showing diffraction angles for electron beam energy E = 137.6eV.

Diffraction Spot	Angle (degrees)	Angle Error (degrees)
1	43.72	0.34
2	43.87	0.38
3	43.83	0.33
4	42.92	0.41
5	41.59	0.35
6	41.97	0.39

Table 6: Table showing diffraction angles for electron beam energy E = 67.3.

Theoretical values for angle of diffraction for each electron energy were calculated using the Bragg theory of diffraction [70]. An Ewald sphere was constructed (using the method outline in section 3.2) for LEED occurring on the Pt(111) surface Equation (21) was used to calculate the de Broglie wavelength of the incident electrons. The incident wavevector was calculated using equation (31) and the Bragg condition is given by equation (32). The (111) plane shows hexagonal symmetry, the plane from which diffraction occurs is given by

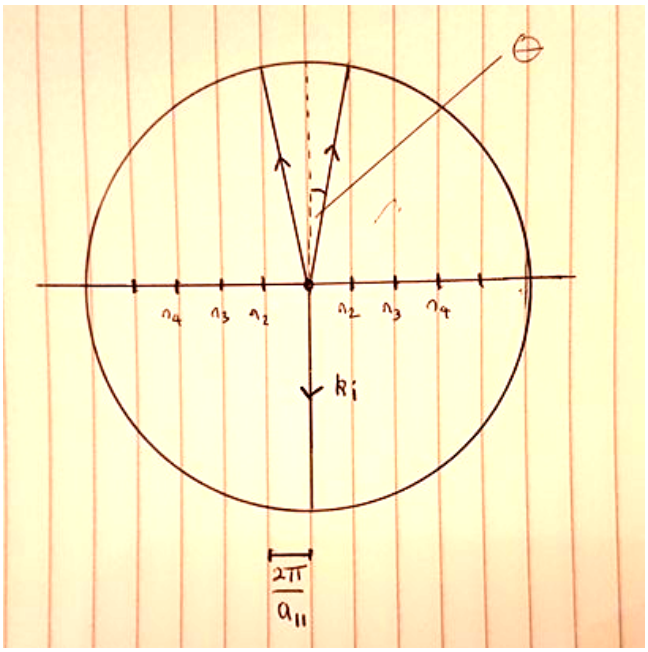

Figure 23: Ewald construction for the Pt(111) surface. The Horizontal line represents the surface of the Pt(111). The k_i vector is the wavevector of the incident electron beam. The vertical pale lines represent the reciprocal lattice rods, each with spacing $\frac{2\pi}{a_\parallel}$

$$a_\parallel = \frac{a}{\sqrt{2}} sin(60) = 2.4\mathring{A} \tag{50}$$

$a_\parallel$ is converted to reciprocal space using the following relationship

$$a^* = \frac{2\pi}{a_\parallel} \tag{51}$$

The angle of diffraction according to Bragg theory was then computed using the relation:

$$\theta = sin^{-1}\left(\frac{a^*}{k}\right) \tag{52}$$

For E = 137.6eV, $\theta = 25.8°$ and for E = 67.3eV, $\theta = 38.4°$

6 Discussion

Three values for the inter-planar spacing for Pt(111) were determined using STM images. Through use of a 3σ consistency check, they were all found to be consistent with a theoretical value for Pt(111) inter-planar spacing. Two

independent values of the same quantity $x_1 \pm \sigma x_1$ and $x_2 \pm \sigma x_2$ are said to be consistent if:

$$| x_1 - x_2 | < 3\sqrt{\sigma x_i^2 + \sigma x_2^2} \tag{53}$$

d_{hkl} $\mathring{A}$	$\lvert x_1$ - $x_2 \rvert$ $\mathring{A}$	$3\sqrt{\sigma x_i^2}$ $\mathring{A}$	Consistent (T/F)
2.24	0.0207	0.78	True
2.29	0.0247	0.556	True
1.91	0.355	1.207	True

Table 7: Table showing consistency checks for the experimentally determined values for inter-planar spacing.

Bright spots in the STM images were indicative of contamination. To reduce contamination the UHV system could be baked out for a longer period of time, at a higher temperature to remove adsorbed gas from the chamber walls. Adsorbed gas could've desorbed over the duration of the experiment and contaminated the surface of the Pt(111). Further measures could be taken by increasing the number of cycles of Ar^+ sputtering to remove contaminants which may have been adsorbed onto the surface of the Pt(111) sample. The bright spots were a major source of error when determining the inter-planar spacing. The line scan was carefully orientated such that bright spots were avoided, to reduce error on the measurements. Another source of error came from noise in the STM images. In this experiment the vacuum pumps were turned off to reduce mechanical noise. Further measure could be taken to reduce noise by increasing the time of STM scanning.

Images of a LEED diffraction pattern for Pt(111) were taken at 136.9eV and 67.3eV. The diffraction patterns showed hexagonal 6-fold symmetry which was consistent with a simulated FCC (111) diffraction pattern generated in LEEDpat4. The angle between the diffraction spots for both LEED patterns was approximately 60 degrees, which was expected. The angle of diffraction for 2 electron beam energies was calculated from the geometry of the experimental setup and from the Bragg diffraction theory. The angles of diffraction derived from the geometry of the setup matched well with the angles of diffraction determined from Bragg theory. An ideal sample to screen value was taken from the Omicrom LEED display specifications. In reality, the sample to screen distance could've been different. If the sample to screen distance was just 4mm smaller, then the angles of diffraction determined from the experimental geometry would be almost exactly the same as the Bragg theory angles. The display to sample distance should be confirmed before the deposition of $BaTiO_3$.

Another source of error which was not directly accounted for in the results comes from the LEED display screen. The display screen in this experiment was hemispherical, calculations for Bragg angles of diffraction were conducted

whilst considering the display screen to be flat. In practice the LEED screen is not perfectly hemispherical, but subtends a solid angle given by

$$\Omega = 2\pi(1 - cos\theta) \tag{54}$$

which is derived from

$$\int_0^\theta 2\pi(Rsin\phi)R \cdot d\phi = 2\pi R^2 \int_0^\theta sin\phi d\phi \tag{55}$$

This creates a problem when measuring the radii of diffraction spots. The radii were measured using straight lines under the assumption that the spots were displayed on a flat plane. The straight lines used to measure the radii of diffraction spots did not account for the variation in height of the diffraction spots, which is caused by the curvature. Theoretically, if we consider a flat display screen in a LEED experiment: incident electrons diffract from the sample surface and are then incident upon the flat display screen. If, however the display screen is hemispherical, the curvature of the screen would cause the diffracted electron beam to be displayed prematurely when compared to the flat screen. Therefore, we can assume that measuring perpendicular distances between diffraction spots on a curved surface, whilst considering it to be flat is a major source of error in this experiment. If the diffraction pattern was centred on the apex of the hemispherical display screen, then the error would not be as large since the greatest curvature occurs at the edges of the screen. In addition to this the Pt(111) sample was mounted onto a manipulator, this would've likely decreased the source to sample distance, affecting the calculated Bragg angles and this was not accounted for in the analysis.

7 Conclusions

A Pt(111) clean surface was prepared for thin film growth. A UHV system was baked out for 48 hours at 160°C. An ultra high vacuum of P = 10^{-9}mbar was made through the use of Ti sublimation pumps, Ion pumps, turbomolecular pumps and a rotary pump. The Pt(111) was cleaned with cycles of 10 minute 3keV Ar^+ sputtering and 20 minutes annealing at 650°C. STM images were taken along with LEED diffraction patterns with incident beam energies E = 67.3eV and E = 136.9eV. The STM images contained bright spots which were indicative of contamination, suggesting that further cleaning should take place. The STM images contained a lot of noise, suggesting that further measures to reduce noise should be taken such as conducting STM scans over a longer period of time and perhaps conducting the scans at a lower temperature. Terrace step heights from STM images confirmed its (111) orientation. The step heights between terraces on STM images were found to be consistent with the inter-planar spacing of a theoretical (111) plane. LEED diffraction patterns showed hexagonal 6-fold symmetry with 60 degree angles between diffraction spots. The LEED diffraction angles were derived from the geometry of the experimental

setup, they were found to be of similar magnitude but not consistent within a 3σ consistency check, suggesting that the sample to display distance should be confirmed before the thin film deposition onto the Pt(111) surface. However, not all sources of error were accounted for such as the curvature of the display screen when measuring the radii of diffraction spots so we can conclude that the Bragg angles of diffraction were consistent within the region of error of the experiment.

References

[1] D. Shechtman, I. Blech, D. Gratias, and J. W. Cahn, "Metallic phase with long-range orientational order and no translational symmetry," *Physical review letters*, vol. 53, no. 20, p. 1951, 1984.

[2] D. Levine and P. J. Steinhardt, "Quasicrystals. i. definition and structure," *Physical Review B*, vol. 34, no. 2, p. 596, 1986.

[3] R. Lifshitz, "The definition of quasicrystals," *arXiv preprint cond-mat/0008152*, 2000.

[4] Förster, "Quasicrystalline structure formation in a classical crystalline thin-film system," *Nature*, vol. 502, no. 7470, p. 215, 2013.

[5] H. Sharma, M. Shimoda, and A. Tsai, "Quasicrystal surfaces: structure and growth of atomic overlayers," *Advances in Physics*, vol. 56, no. 3, pp. 403–464, 2007.

[6] J.-M. Dubois, "Properties-and applications of quasicrystals and complex metallic alloys," *Chemical Society Reviews*, vol. 41, no. 20, pp. 6760–6777, 2012.

[7] L. H, "Surfaces and interfaces of solids."

[8] C. Sire and D. Gratias, "Introduction to the physics of quasicrystals," pp. 127–154, 01 1994.

[9] B. Grünbaum and G. C. Shephard, *Tilings and patterns*. Freeman, 1987.

[10] F. Ardila and R. P. Stanley, "Tilings," *The Mathematical Intelligencer*, vol. 32, no. 4, pp. 32–43, 2010.

[11] T. Janssen, "Crystallography of quasi-crystals," *Acta Crystallographica Section A: Foundations of Crystallography*, vol. 42, no. 4, pp. 261–271, 1986.

[12] H.-C. Jeong and P. J. Steinhardt, "Constructing penrose-like tilings from a single prototile and the implications for quasicrystals," *Physical Review B*, vol. 55, no. 6, p. 3520, 1997.

[13] V. O. HEALEY, "A modification of the penrose aperiodic tiling."

[14] P. J. Steinhardt, "New perspectives on forbidden symmetries, quasicrystals, and penrose tilings," *Proceedings of the National Academy of Sciences*, vol. 93, no. 25, pp. 14 267–14 270, 1996.

[15] P. J. Steinhardt and H.-C. Jeong, "A simpler approach to penrose tiling with implications for quasicrystal formation," *Nature*, vol. 382, no. 6590, p. 431, 1996.

[16] T. Ishimasa, H.-U. Nissen, and Y. Fukano, "New ordered state between crystalline and amorphous in ni-cr particles," *Phys. Rev. Lett.*, vol. 55, pp. 511–513, Jul 1985. [Online]. Available: https://link.aps.org/doi/10.1103/PhysRevLett.55.511

[17] N. Niizeki and H. Mitani, "Two-dimensional dodecagonal quasilattices," *Journal of Physics A: Mathematical and General*, vol. 20, no. 6, p. L405, 1987.

[18] F. Bechstedt, *Principles of surface physics*. Springer Science & Business Media, 2012.

[19] J. Y. Tsao, *Materials fundamentals of molecular beam epitaxy*. Academic Press, 2012.

[20] J. F. Nicholas, "2.1.1.5.1 the terrace-ledge-kink (tlk) model: Datasheet from landolt-börnstein - group iii condensed matter · volume 24a: "structure" in springermaterials (https://dx.doi.org/10.1007/10031427_13)," copyright 1993 Springer-Verlag Berlin Heidelberg. [Online]. Available: https://materials.springer.com/lb/docs/sm_lbs_978-3-540-47397-8_13

[21] P. Zieliński, "Review of surface relaxation and reconstruction phenomena," *Acta Physica Polonica A*, vol. 89, no. 2, pp. 251–263, 1996.

[22] M. H. Feng Liu and M. Lagally, "Surfaces and interfaces, structure of," *Encyclopedia of Applied Physics*, p. 321, 1999.

[23] W. Kohn and L. J. Sham, "Self-consistent equations including exchange and correlation effects," *Physical review*, vol. 140, no. 4A, p. A1133, 1965.

[24] J. Inglesfield, "Surface electronic structure," *Reports on Progress in Physics*, vol. 45, no. 3, p. 223, 1982.

[25] H. Brune, "Physical properties of thin films and artificial multilayers," *Encyclopedia of Materials: Science and Technology*, pp. 3683–3693, 2001.

[26] G. Biasiol and L. Sorba, "Molecular beam epitaxy: principles and applications," *Crystal growth of materials for energy production and energy-saving applications*, pp. 66–83, 2001.

[27] F. Rinaldi, "Basics of molecular beam epitaxy (mbe)," *Annual Report*, pp. 1–8, 2002.

[28] U. D. of Transportation Federal Aviation Administration, "Handbook, airplane flying," *1999 Annual Report*, p. Chapter 14, 2004.

[29] J. Golinval, "Mechanical design of turbomachinery," *University of Liege, Belgium*, 2013.

[30] P. C. Lucas, "Materials physics lectures," *University of Liverpool*, 2017.

[31] H. Cohrt and F. Thümmler, "Degradation mechanisms of thermal barrier coatings in bending tests," *Surface and Coatings Technology*, vol. 32, no. 1-4, pp. 339–348, 1987.

[32] D. Bae, Y. Kim, and I. Kim, "Thermally stable quasicrystalline phase in a superplastic mg–zn–y–zr alloy," *Materials Letters*, vol. 60, no. 17-18, pp. 2190–2193, 2006.

[33] B. Sakintuna, F. Lamari-Darkrim, and M. Hirscher, "Metal hydride materials for solid hydrogen storage: a review," *International journal of hydrogen energy*, vol. 32, no. 9, pp. 1121–1140, 2007.

[34] K. Kelton and P. Gibbons, "Hydrogen storage in quasicrystals," *MRS Bulletin*, vol. 22, no. 11, p. 69–72, 1997.

[35] R. Stroud, A. Viano, P. Gibbons, K. Kelton, and S. Misture, "Stable ti-based quasicrystal offers prospect for improved hydrogen storage," *Applied physics letters*, vol. 69, no. 20, pp. 2998–3000, 1996.

[36] Y. Margoninski, "1. ultra-high vacuum systems for surface research," *Vacuum*, vol. 28, no. 12, pp. 515–521, 1978.

[37] O. L. Vacuum, "Fundamentals of vacuum technology, 00.200. 02, kat," *Nr*, vol. 199, p. 90, 2007.

[38] G. Lewin and A. M. Russell, "Fundamentals of vacuum science and technology," *American Journal of Physics*, vol. 33, pp. 977–977, 1965.

[39] J. L. de Segovia, "Physics of outgassing," 1999.

[40] D. J. Santeler, "Estimating the gas partial pressure due to diffusive outgassing," *Journal of Vacuum Science & Technology A: Vacuum, Surfaces, and Films*, vol. 10, no. 4, pp. 1879–1883, 1992.

[41] W. Kauzmann, *Kinetic theory of gases*. Courier Corporation, 2012.

[42] H. Semat and R. Katz, "Physics, chapter 16: Kinetic theory of gases," 1958.

[43] C. Hammill, "Outgassing of stainless steel vacuum chambers and the vacuum pumping performance evaluation of a titanium sublimation pump."

[44] B. S. S. Association *et al.*, "Melting temperature ranges for stainless steels," *author unknown, published at http://www. bssa. org. uk/topics. php*.

[45] V. Pfeiffer, *The Vacuum Technology Book Volume II*. Pfeiffer Vacuum GmbH, 2013.

[46] M. Iqbal, "Design modification in rotor blade of turbo molecular pump," *Nuclear Instruments and Methods in Physics Research A*, vol. 678, pp. 88–90, 2012.

[47] L. Nelik, *Centrifugal and Rotary Pumps*. CRC Press, 1999.

[48] M. Lowe, "Surface studies of model intermetallic catalysts," *PhD Thesis, University of Liverpool*, 2015.

[49] M. v. Pirani, "Selbstzeigendes vakuum-messinstrument," *Verhandl. deut. Physik Ges*, vol. 8, p. 686, 1906.

[50] J.-S. Shie, B. C. Chou, and Y.-M. Chen, "High performance pirani vacuum gauge," *Journal of Vacuum Science & Technology A: Vacuum, Surfaces, and Films*, vol. 13, no. 6, pp. 2972–2979, 1995.

[51] E. L. Pace, "Scientific foundations of vacuum technique (dushman, saul)," *Journal of Chemical Education*, vol. 39, no. 8, p. A606, 1962. [Online]. Available: https://doi.org/10.1021/ed039pA606

[52] F. Jona, J. Strozier Jr, and W. Yang, "Low-energy electron diffraction for surface structure analysis," *Reports on Progress in Physics*, vol. 45, no. 5, p. 527, 1982.

[53] H. Ibach, *Physics of surfaces and interfaces*. Springer, 2006, vol. 12.

[54] A. Zangwill, *Physics at surfaces*. Cambridge university press, 1988.

[55] G. Binnig, H. Rohrer, C. Gerber, and E. Weibel, "Tunneling through a controllable vacuum gap," *Applied Physics Letters*, vol. 40, no. 2, pp. 178–180, 1982.

[56] C. J. Chen, *Introduction to scanning tunneling microscopy*. Oxford University Press on Demand, 1993, vol. 4.

[57] S. Lounis, "Theory of scanning tunneling microscopy," *arXiv preprint cond-mat/1404096*, 2014.

[58] C. Krull, *Electronic structure of metal phthalocyanines on Ag (100)*. Springer Science & Business Media, 2013.

[59] B. Bhushan and O. Marti, "Scanning probe microscopy–principle of operation, instrumentation, and probes," in *Springer Handbook of Nanotechnology*. Springer, 2004, pp. 325–369.

[60] Z. Papadopolos, G. Kasner, J. Ledieu, E. J. Cox, N. V. Richardson, Q. Chen, R. D. Diehl, T. A. Lograsso, A. R. Ross, and R. McGrath, "Bulk termination of the quasicrystalline fivefold surface of $\mathrm{al_{70}pd_{21}mn_9}$," *Phys. Rev. B*, vol. 66, p. 184207, Nov 2002. [Online]. Available: https://link.aps.org/doi/10.1103/PhysRevB.66.184207

[61] R. Parsons, "Sputter deposition processes," *Thin film processes II*, vol. 2, p. 177, 1991.

[62] J. Bohdansky, "A universal relation for the sputtering yield of monatomic solids at normal ion incidence," *Nuclear Instruments and Methods in Physics Research Section B: Beam Interactions with Materials and Atoms*, vol. 2, no. 1-3, pp. 587–591, 1984.

[63] T. G. Digges, S. J. Rosenberg, and G. W. Geil, "Heat treatment and properties of iron and steel," NATIONAL BUREAU OF STANDARDS GAITHERSBURG MD, Tech. Rep., 1966.

[64] S. Sastry, "Ohmic heating," *Food Engineering*, vol. 3.

[65] P. Richardson, *Thermal technologies in food processing*. Taylor & Francis, 2001.

[66] J. Arblaster, "Crystallographic properties of platinum," *Platinum Metals Review*, vol. 41, no. 1, pp. 12–21, 1997.

[67] J. G.-R. J. C. J. G.-H. I. Horcas, R. Fernández and A. Baró, "Wsxm: A software for scanning probe microscopy and a tool for nanotechnology," *Review of Scientific Instruments*, vol. 78, no. 013705, 2007.

[68] D. K. Hermann and D. M. A. V. Hove, "Pc-based software tool to visualize and analyze leed patterns of substrates and overlayers." [Online]. Available: http://www.fhi-berlin.mpg.de/KHsoftware/LEEDpat/index.html

[69] C. A. Schneider, W. S. Rasband, and K. W. Eliceiri, "Nih image to imagej: 25 years of image analysis," *Nature methods*, vol. 9, no. 7, p. 671, 2012.

[70] K. M. Oliver, "Surface analysis of the ag-in-yb 1/1 quasicrystal approximant," *Masters Thesis*, 2012.

A Analysis and Error Calculations

3σ consistency checks were carried out using the equation:

$$\mid x_1 - x_2 \mid < 3\sqrt{\sigma x_i^2 + \sigma x_2^2} \tag{56}$$

In section 5.1 data from WSxM was exported to Microsoft excel. The mean Z value was then calculated. The error on the mean Z value is given by the standard deviation:

$$\sigma Z = \sqrt{\frac{\sum_{i=1}^{n} x_i - \overline{x}}{N-1}} \tag{57}$$

The average Z values betweens steps are then calculated, their errors are given by the sum of their errors in quadrature

$$\sigma d_{hkl} = \sqrt{\sigma Z_1^2 + \sigma Z_2^2} \tag{58}$$

The angle between diffraction spots in the LEED images were recorded multiple times to reduce error. The mean angle was taken and its error is given by the standard deviation:

$$\sigma\theta = \sqrt{\frac{\sum_{i=1}^{n} \theta_i - \overline{\theta}}{N-1}} \tag{59}$$

To determine the pixels per meter of the image, the diameter of the screen was measured in pixels across the image in ImageJ. Multiple attempts were made and the mean diameter was calculated by taking the difference in the x coordinates on either side of the screen ($x_i - x_f$). The error is given by

$$\sigma d = {\sigma x_i}^2 + {\sigma x_f}^2 \tag{60}$$

The number of Pixels per meter was calculated by dividing the screen diameter by the pixel diameter measured in ImageJ. Its error is calculated by divided the error of the pixel diameter by the screen diameter in meters

$$\sigma Pixelspermeter = \frac{\sigma d}{d} \tag{61}$$

The radius of diffraction spots (equation 46) has an error given by

$$\sigma|r| = \sqrt{\frac{{x_f - x_i}^2}{|r|}{\sigma x_f}^2 + \frac{{x_f - x_i}^2}{|r|}{\sigma x_i}^2 + \frac{{y_f - y_i}^2}{|r|}{\sigma y_f}^2 + \frac{{y_f - y_i}^2}{|r|}{\sigma y_i}^2} \tag{62}$$

The radii of the diffraction spots are then converted from pixels to meters, the error is given by

$$\sigma r(m) = r(m)\sqrt{\frac{{\sigma d}^2}{d} + \frac{{\sigma r}^2}{r}} \tag{63}$$

Finally, r $\pm$ σr and d $\pm \sigma d$ are used to calculate the angle of diffraction, given by equation (47), its error is:

$$\sigma\theta = \sqrt{\frac{\sqrt{d^2}}{d\sqrt{d^2 - r^2}}^2 \sigma r^2} \tag{64}$$

B Raw Data and Additional Information

This section contains all raw data used and relevant information which is not present in the main body of the project report

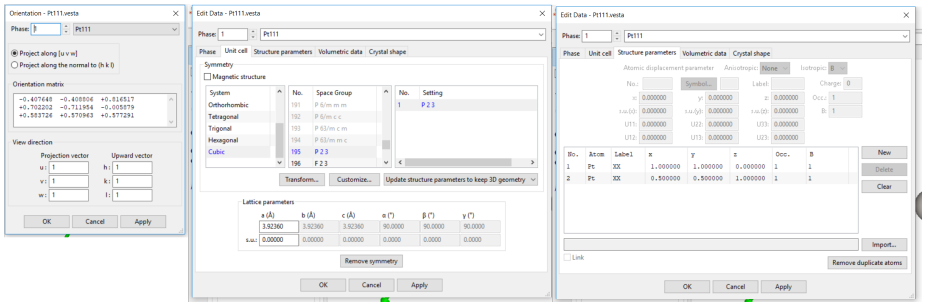

Figure 24: A screenshot showing the model setup for Pt(111) in VESTA

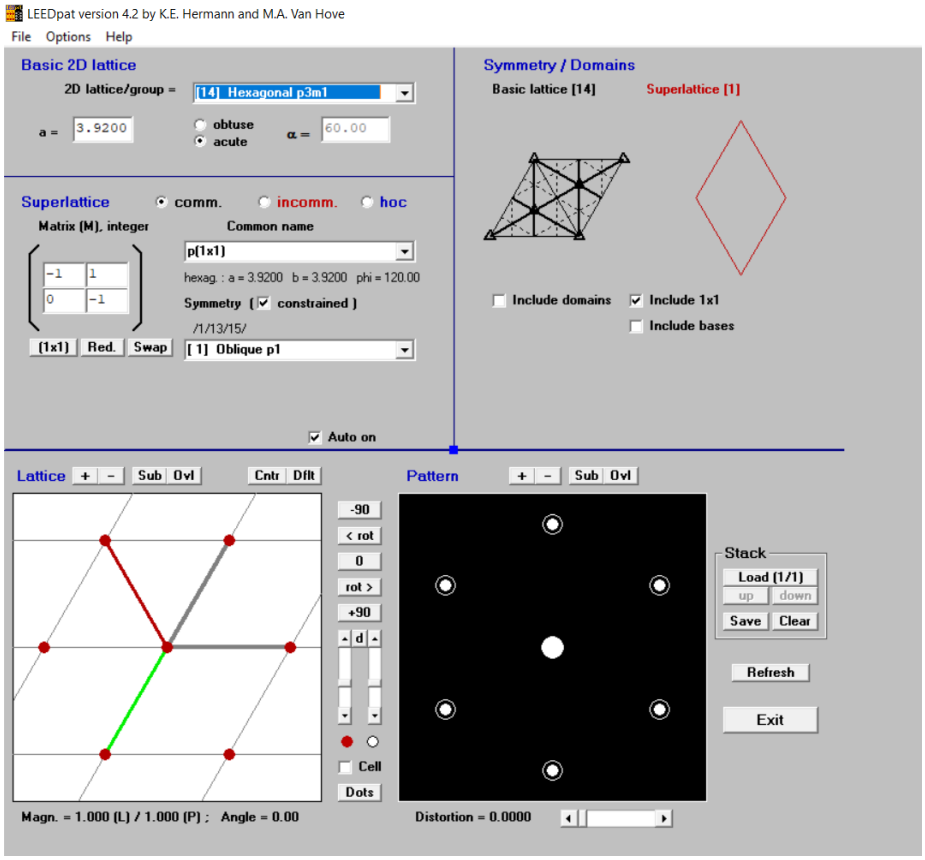

Figure 25: LEED-pat4 setup used to generate the simulated LEED pattern.

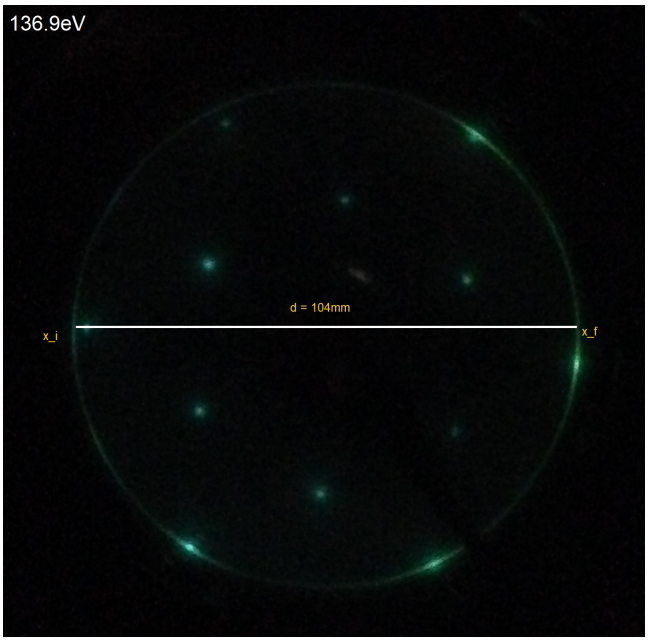

Figure 26: Pixel measurments used to calculate the pixels per meter in the LEED images. Repeated measures were used to reduce error but only 1 example is shown here.

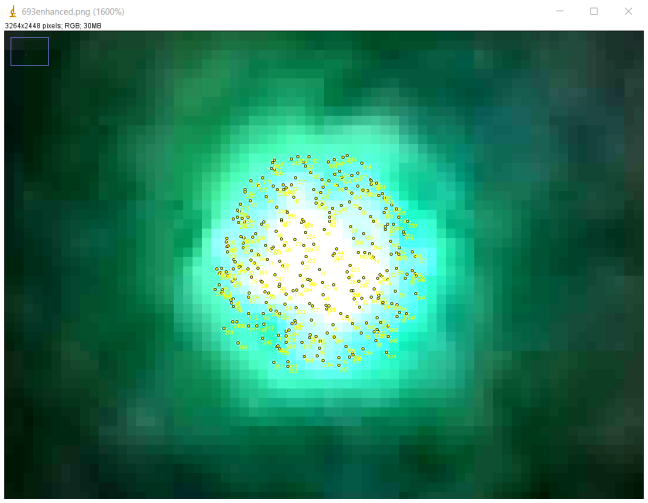

Figure 27: An example of how the ImageJ multispot tool works. Many points were selected across diffraction spots and ImageJ determines the mean coordinates for x and y across the diffraction spot.

Reading Attempt	x_i (pixel)	x_f (pixel)
1	165	1301
2	167	1303
3	163	1303
4	165	1301
5	163	1303
6	165	1307
7	163	1303
8	165	1301
9	163	1301
10	163	1303
Mean	Value	Error
x_i (pixel)	164.2	1.326649916
x_f (pixel)	1302.6	1.743559577
diameter (pixel)	1138.4	2.19089023
diameter (mm)	0.104	0
Pixels per m	10946.15385	0.000200152

(1) 1 Data accumalated to calculate the number of pixels per meter

Reading Attempt	Points	Angle (degrees)
1	1 to 2	60.25
2	1 to 2	60.85
3	1 to 2	59.11
Reading Attempt	Points	Angle (degrees)
1	2 to 3	60.1
2	2 to 3	60.21
3	2 to 3	60
Reading Attempt	Points	Angle (degrees)
1	3 to 4	59.5
2	3 to 4	60.47
3	3 to 4	60.66
Reading Attempt	Points	Angle (degrees)
1	4 to 5	60.54
2	4 to 5	59.25
3	4 to 5	60.11
Reading Attempt	Points	Angle (degrees)
1	5 to 6	59.16
2	5 to 6	60.02
3	5 to 6	60.16

(1) 2 Readings taken from the ImageJ program to calculate the angle between diffraction spots in the LEED diffraction patterns.

The xyz data taken from WSxM to calculate terrace height differences for STM image 1.

X-plane (nm)	Y-plane (nm)	Z-plane (Amstrong)
86.65362	35.459883	1.324381
86.418787	35.694716	1.649046
86.183953	35.92955	1.473775
85.949119	35.92955	1.530412
85.714286	36.164384	1.552387
85.479452	36.399217	1.605889
85.244618	36.634051	1.613368
85.009785	36.868885	1.726008
84.774951	36.868885	1.770993
84.540117	37.103718	1.748914
84.305284	37.338552	1.686192
84.07045	37.573386	1.771263
83.835616	37.808219	1.400735
83.600783	37.808219	1.381487
83.365949	38.043053	1.480747
83.131115	38.277886	1.803708
82.896282	38.51272	1.522423
82.661448	38.51272	1.505449
82.426614	38.747554	1.84603
82.191781	38.982387	1.789561
81.956947	39.217221	1.765493
81.722114	39.452055	1.741709
81.48728	39.452055	1.752872
81.252446	39.686888	1.706329
81.017613	39.921722	1.779179
80.782779	40.156556	1.704236
80.547945	40.391389	1.969784
80.313112	40.391389	1.967589
80.078278	40.626223	1.982742
79.843444	40.861057	1.834756
79.608611	41.09589	1.813245
79.373777	41.330724	1.865042
79.138943	41.330724	1.863131
78.90411	41.565558	1.600889
78.669276	41.800391	1.539873
78.434442	42.035225	1.615849
78.199609	42.270059	1.910671
77.964775	42.270059	2.014489
77.729941	42.504892	2.135655
77.495108	42.739726	1.702315
77.260274	42.97456	1.68391
77.02544	43.209393	1.863625
76.790607	43.209393	1.908325
76.555773	43.444227	1.947069
76.320939	43.679061	1.698185
76.086106	43.913894	1.554178
75.851272	44.148728	1.636122
75.616438	44.148728	1.68196
75.381605	44.383562	2.165502
75.146771	44.618395	2.16614
74.911937	44.853229	2.181293
74.677104	44.853229	2.096107
74.44227	45.088063	1.965173
74.207436	45.322896	2.034043
73.972603	45.55773	1.938068
73.737769	45.792564	1.73068
73.502935	45.792564	1.710011
73.268102	46.027397	1.845104
73.033268	46.262231	1.34952
72.798434	46.497065	1.627838
72.563601	46.731898	1.556589
72.328767	46.731898	1.432181
72.093933	46.966732	1.44705
71.8591	47.201566	1.304464
71.624266	47.436399	1.611508
71.389432	47.671233	1.479437
71.154599	47.671233	1.552843
70.919765	47.906067	1.65923
70.684932	48.1409	1.551013
70.450098	48.375734	1.653421
70.215264	48.610568	1.744745
69.980431	48.610568	1.705317
69.745597	48.845401	1.464392
69.510763	49.080235	1.676507
69.27593	49.315068	1.845138
69.041096	49.549902	1.449598
68.806262	49.549902	1.510215
68.571429	49.784736	1.490957
68.336595	50.019569	1.56267
68.101761	50.254403	1.561908
67.866928	50.254403	1.520206
67.632094	50.489237	1.703332
67.39726	50.72407	1.554208
67.162427	50.958904	1.745292
66.927593	51.193738	1.71895
66.692759	51.193738	1.736934
66.457926	51.428571	1.824826

66.223092	51.663405	1.831453
65.988258	51.898239	1.89265
65.753425	52.133072	1.835612
65.518591	52.133072	1.814943
65.283757	52.367906	1.877845
65.048924	52.60274	1.980253
64.81409	52.837573	1.913836
64.579256	53.072407	1.82324
64.344423	53.072407	1.759938
64.109589	53.307241	1.87002
63.874755	53.542074	2.039504
63.639922	53.776908	2.033909
63.405088	54.011742	2.17156
63.170254	54.011742	2.007361
62.935421	54.246575	1.993241
62.700587	54.481409	1.901529
62.465753	54.716243	1.796743
62.23092	54.951076	1.747074
61.996086	54.951076	1.744311
61.761252	55.18591	1.629577
61.526419	55.420744	1.646436
61.291585	55.655577	1.627484
61.056751	55.890411	1.660827
60.821918	55.890411	1.600652
60.587084	56.125245	1.881548
60.35225	56.360078	1.960082
60.117417	56.594912	1.750115
59.882583	56.594912	1.766109
59.64775	56.829746	2.084806
59.412916	57.064579	1.897598
59.178082	57.299413	1.793949
58.943249	57.534247	1.862251
58.708415	57.534247	1.908372
58.473581	57.76908	1.701837
58.238748	58.003914	1.819308
58.003914	58.238748	2.207333
57.76908	58.473581	2.30832
57.534247	58.473581	2.134742
57.299413	58.708415	2.037915
57.064579	58.943249	2.163913
57.064579	58.943249	2.163913
57.299413	59.178082	2.396335
57.299413	59.412916	2.176932
57.534247	59.64775	2.01003
57.76908	59.882583	1.995731

57.76908	60.117417	1.856477
58.003914	60.35225	2.028362
58.238748	60.587084	1.978841
58.238748	60.821918	1.728174
58.473581	61.056751	1.725834
58.708415	61.291585	1.890613
58.708415	61.526419	2.031291
58.943249	61.761252	2.01275
59.178082	61.996086	1.945324
59.178082	62.23092	2.000758
59.412916	62.465753	1.962322
59.64775	62.700587	1.793999
59.64775	62.935421	1.718125
59.882583	63.170254	2.026412
59.882583	63.170254	2.026412
59.64775	63.405088	1.972501
59.64775	63.639922	1.903733
59.412916	63.874755	1.906949
59.178082	64.109589	1.936598
59.178082	64.344423	1.867261
58.943249	64.579256	1.73178
58.708415	64.81409	1.875683
58.708415	65.048924	1.812294
58.473581	65.283757	1.83569
58.238748	65.518591	1.823274
58.238748	65.753425	1.844318
58.003914	65.988258	1.526654
58.003914	66.223092	1.226249
57.76908	66.457926	0.544504
57.534247	66.692759	-0.081556
57.534247	66.927593	-0.336487
57.299413	67.162427	-0.439283
57.064579	67.39726	0.019248
57.064579	67.632094	-0.115174
56.829746	67.866928	-0.219392
56.594912	68.101761	-0.61152
56.594912	68.336595	-0.414283
56.360078	68.571429	-0.446594
56.125245	68.806262	-0.508463
56.125245	69.041096	-0.553642
55.890411	69.27593	-0.479939
55.655577	69.510763	-0.503155
55.655577	69.745597	-0.386899
55.420744	69.980431	-0.405019
55.18591	70.215264	-0.616671

55.18591	70.450098	-0.475119
54.951076	70.684932	-0.568252
54.951076	70.919765	-0.564545
54.716243	71.154599	-0.697184
54.481409	71.389432	-0.531112
54.481409	71.624266	-0.579438
54.246575	71.8591	-0.538989
54.011742	72.093933	-0.382011
54.011742	72.328767	-0.569867
53.776908	72.563601	-0.586829
53.776908	72.563601	-0.586829
54.011742	72.563601	-0.598845
54.246575	72.798434	-0.308442
54.481409	72.798434	-0.291468
54.716243	72.798434	-0.305757
54.951076	73.033268	-0.496249
55.18591	73.033268	-0.514801
55.420744	73.268102	-0.652734
55.655577	73.268102	-0.541115
55.890411	73.268102	-0.52073
56.125245	73.502935	-0.566839
56.360078	73.502935	-0.639961
56.594912	73.502935	-0.613892
56.829746	73.737769	-0.507946
57.064579	73.737769	-0.537583
57.299413	73.737769	-0.539082
57.534247	73.972603	-0.824502
57.76908	73.972603	-1.023248
58.003914	73.972603	-1.282816
58.238748	74.207436	-1.558004
58.473581	74.207436	-1.793982
58.708415	74.44227	-2.265848
58.943249	74.44227	-2.44072
59.178082	74.44227	-2.56159
59.412916	74.677104	-2.529256
59.64775	74.677104	-2.559746
59.882583	74.677104	-2.56494
60.117417	74.911937	-2.524932
60.35225	74.911937	-2.447135
60.587084	74.911937	-2.367064
60.821918	75.146771	-2.641137
61.056751	75.146771	-2.654858
61.291585	75.146771	-2.735085
61.526419	75.381605	-2.872997
61.761252	75.381605	-2.868243

61.996086	75.616438	-2.856089
62.23092	75.616438	-2.835988
62.465753	75.616438	-2.934689
62.700587	75.851272	-2.631213
62.935421	75.851272	-2.605996
63.170254	75.851272	-2.501198
63.405088	76.086106	-2.737449
63.639922	76.086106	-2.800623
63.874755	76.086106	-2.885682
64.109589	76.320939	-2.983804
64.344423	76.320939	-2.970524
64.579256	76.320939	-2.910917
64.81409	76.555773	-2.707769
65.048924	76.555773	-2.526517
65.283757	76.790607	-2.369717
65.518591	76.790607	-2.450513
65.753425	76.790607	-2.556888
65.988258	77.02544	-2.770401
66.223092	77.02544	-2.720458
66.457926	77.02544	-2.701209
66.692759	77.260274	-2.879195
66.927593	77.260274	-2.844884
67.162427	77.260274	-2.711949
67.39726	77.495108	-2.941094
67.632094	77.495108	-2.884329
67.866928	77.495108	-2.868491
68.101761	77.729941	-2.890158
68.336595	77.729941	-2.893363
68.571429	77.964775	-3.025306
68.806262	77.964775	-2.96513
69.041096	77.964775	-2.902681
69.27593	78.199609	-2.878874
69.510763	78.199609	-2.835751
69.745597	78.199609	-2.755112
69.980431	78.434442	-2.66624
70.215264	78.434442	-2.666034
70.215264	78.434442	-2.666034
69.980431	78.669276	-2.683849
69.745597	78.90411	-2.704791
69.510763	78.90411	-2.677997
69.27593	79.138943	-2.678475
69.041096	79.373777	-2.896379
68.806262	79.608611	-2.96848
68.571429	79.843444	-2.882556
68.336595	80.078278	-2.806886

68.101761	80.078278	-2.769859
67.866928	80.313112	-2.987479
67.632094	80.547945	-2.85267
67.39726	80.782779	-2.723546
67.162427	81.017613	-2.431281
66.927593	81.017613	-2.496288
66.692759	81.252446	-2.558157
66.457926	81.48728	-2.739113
66.223092	81.722114	-2.733359
65.988258	81.956947	-2.783576
65.753425	82.191781	-2.866193
65.518591	82.191781	-2.802734
65.283757	82.426614	-2.701463
65.048924	82.661448	-2.888103
64.81409	82.896282	-2.906487
64.579256	83.131115	-3.051347
64.344423	83.131115	-3.048142
64.109589	83.365949	-2.847132
63.874755	83.600783	-2.785935
63.639922	83.835616	-2.730139
63.405088	84.07045	-2.888073
63.170254	84.305284	-2.743601
62.935421	84.305284	-2.770807
62.700587	84.540117	-2.709042
62.465753	84.774951	-2.460831

The xyz data taken from WSxM analysis of STM image 2, used for calculating the interplanar spacings from the terrace height differences.

X-plane (nm)	Y-plane (nm)	Z-plane (Amstrong)
2.58317	51.663405	-3.20929
2.818004	51.663405	-3.049785
3.052838	51.663405	-2.970003
3.287671	51.663405	-2.987138
3.522505	51.663405	-2.948852
3.757339	51.663405	-3.295964
3.992172	51.663405	-3.225277
4.227006	51.663405	-2.684494
4.46184	51.663405	-1.734153
4.696673	51.663405	-1.434245
4.931507	51.663405	-1.078061
5.166341	51.663405	-0.942856
5.401174	51.663405	-0.658721
5.636008	51.663405	-0.587608
5.870841	51.663405	-0.794459
6.105675	51.663405	-0.632395
6.340509	51.663405	-0.611304
6.575342	51.898239	-1.020411
6.810176	51.898239	-0.716239
7.04501	51.898239	-0.703674
7.279843	51.898239	-0.939089
7.514677	51.898239	-0.703556
7.749511	51.898239	-0.682322
7.984344	51.898239	-0.722195
8.219178	51.898239	-0.582443
8.454012	51.898239	-0.536056
8.688845	51.898239	-0.706527
8.923679	51.898239	-0.82186
9.158513	51.898239	-0.385811
9.393346	51.898239	-0.718571
9.62818	51.898239	-0.818698
9.863014	51.898239	-0.778564
10.097847	51.898239	-0.690113
10.332681	51.898239	-0.652679
10.567515	51.898239	-0.749822
10.802348	51.898239	-0.917025
11.037182	51.898239	-0.738051
11.272016	51.898239	-0.416825
11.506849	51.898239	-0.294979
11.741683	51.898239	-0.418981
11.976517	51.898239	-0.66008
12.21135	51.898239	-0.760207
12.446184	51.898239	-0.809459
12.681018	51.898239	-0.788652
12.915851	51.898239	-0.600014
13.150685	51.898239	-0.696163
13.385519	51.898239	-0.627465
13.620352	51.898239	-0.887322
13.855186	51.898239	-1.143485
14.09002	52.133072	-0.929588
14.324853	52.133072	-0.650285
14.559687	52.133072	-0.746291
14.794521	52.133072	-0.657272
15.029354	52.133072	-0.726703
15.264188	52.133072	-0.770414
15.499022	52.133072	-0.889441
15.733855	52.133072	-0.81918
15.968689	52.133072	-0.960235
16.203523	52.133072	-0.814088
16.438356	52.133072	-0.54459
16.67319	52.133072	-0.678397
16.908023	52.133072	-0.634995
17.142857	52.133072	-0.546402
17.377691	52.133072	-1.003933
17.612524	52.133072	-1.190462
17.847358	52.133072	-0.911869
18.082192	52.133072	-0.487331
18.317025	52.133072	-0.628244
18.551859	52.133072	-0.527998
18.786693	52.133072	-0.409704
19.021526	52.133072	-0.822471
19.25636	52.133072	-1.182231
19.491194	52.133072	-1.139112
19.726027	52.133072	-0.946638
19.960861	52.133072	-0.710394
20.195695	52.133072	-0.911702
20.430528	52.133072	-1.211777
20.665362	52.133072	-1.023139
20.900196	52.133072	-0.888361
21.135029	52.133072	-0.943866
21.369863	52.133072	-0.929596
21.604697	52.133072	-0.991353
21.83953	52.367906	-0.73994
22.074364	52.367906	-0.668399
22.309198	52.367906	-1.072782

22.544031	52.367906	-0.80641
22.778865	52.367906	-0.328013
23.013699	52.367906	-0.617145
23.248532	52.367906	-0.81547
23.483366	52.367906	-0.944729
23.7182	52.367906	-0.784513
23.953033	52.367906	-0.569443
24.187867	52.367906	-0.664881
24.422701	52.367906	-0.629721
24.657534	52.367906	-0.883041
24.892368	52.367906	-0.586685
25.127202	52.367906	-0.640627
25.362035	52.367906	-0.72228
25.596869	52.367906	-0.787449
25.831703	52.367906	-0.880471
26.066536	52.367906	-0.910823
26.30137	52.367906	-1.018198
26.536204	52.367906	-0.833397
26.771037	52.367906	-0.94333
27.005871	52.367906	-0.882022
27.240705	52.367906	-0.774386
27.475538	52.367906	-0.980384
27.710372	52.367906	-1.013436
27.945205	52.367906	-1.012666
28.180039	52.367906	-0.999817
28.414873	52.367906	-0.760163
28.649706	52.367906	-0.855316
28.88454	52.367906	-1.04554
29.119374	52.367906	-1.13103
29.354207	52.367906	-0.995257
29.589041	52.60274	-0.528691
29.823875	52.60274	-0.28861
30.058708	52.60274	-0.579731
30.293542	52.60274	-0.768818
30.528376	52.60274	-0.876193
30.763209	52.60274	-1.165467
30.998043	52.60274	-1.031684
31.232877	52.60274	-1.072978
31.46771	52.60274	-1.183337
31.702544	52.60274	-1.205873
31.937378	52.60274	-1.082748
32.172211	52.60274	-1.344026
32.407045	52.60274	-0.975621
32.641879	52.60274	-0.847237
32.876712	52.60274	-1.090326

33.111546	52.60274	-1.13432
33.34638	52.60274	-0.994142
33.581213	52.60274	-0.766282
33.816047	52.60274	-0.702558
34.050881	52.60274	-0.939252
34.285714	52.60274	-1.201952
34.520548	52.60274	-1.182708
34.755382	52.60274	-1.211212
34.990215	52.60274	-1.081976
35.225049	52.60274	-1.275327
35.459883	52.60274	-1.338221
35.694716	52.60274	-1.324093
35.92955	52.60274	-1.39523
36.164384	52.60274	-1.048994
36.399217	52.60274	-1.131074
36.634051	52.60274	-1.307371
36.868885	52.60274	-1.167903
37.103718	52.837573	-1.74072
37.338552	52.837573	-1.510018
37.573386	52.837573	-1.562681
37.808219	52.837573	-1.461298
38.043053	52.837573	-1.545936
38.277886	52.837573	-1.098376
38.51272	52.837573	-0.409232
38.747554	52.837573	0.060923
38.982387	52.837573	1.25427
39.217221	52.837573	1.038892
39.452055	52.837573	1.25112
39.686888	52.837573	1.867505
39.921722	52.837573	1.73455
40.156556	52.837573	1.220603
40.391389	52.837573	1.127581
40.626223	52.837573	1.446248
40.861057	52.837573	1.506703
41.09589	52.837573	1.547122
41.330724	52.837573	1.41232
41.565558	52.837573	1.386657
41.800391	52.837573	1.271182
42.035225	52.837573	1.214256
42.270059	52.837573	1.150367
42.504892	52.837573	1.222333
42.739726	52.837573	1.378428
42.97456	52.837573	1.316101
43.209393	52.837573	1.253633
43.444227	52.837573	1.181785

43.679061	52.837573	1.217656
43.913894	52.837573	1.257932
44.148728	52.837573	1.079645
44.383562	52.837573	1.054835
44.618395	52.837573	1.332717
44.853229	53.072407	1.140325
45.088063	53.072407	1.547668
45.322896	53.072407	1.353039
45.55773	53.072407	1.210421
45.792564	53.072407	1.318483
46.027397	53.072407	1.011019
46.262231	53.072407	1.105581
46.497065	53.072407	1.21279
46.731898	53.072407	1.334494
46.966732	53.072407	1.2797
47.201566	53.072407	0.966694
47.436399	53.072407	0.892288
47.671233	53.072407	0.912385
47.906067	53.072407	0.922392
48.1409	53.072407	1.041822
48.375734	53.072407	1.20417
48.610568	53.072407	1.097932
48.845401	53.072407	0.872891
49.080235	53.072407	0.805307
49.315068	53.072407	0.665389
49.549902	53.072407	0.587288
49.784736	53.072407	0.961236
50.019569	53.072407	0.950921
50.254403	53.072407	0.881774
50.489237	53.072407	0.861653
50.72407	53.072407	0.773179
50.958904	53.072407	0.710568
51.193738	53.072407	0.739476
51.428571	53.072407	0.743799
51.663405	53.072407	0.751674
51.898239	53.072407	0.99275
52.133072	53.072407	1.243915
52.367906	53.072407	1.082397
52.60274	53.307241	0.628383
52.837573	53.307241	0.73005
53.072407	53.307241	1.088366
53.307241	53.307241	1.060572
53.542074	53.307241	1.042725
53.776908	53.307241	0.788836
54.011742	53.307241	0.625613
54.246575	53.307241	0.536854
54.481409	53.307241	0.689538
54.716243	53.307241	0.890397
54.951076	53.307241	0.917599
55.18591	53.307241	0.732917
55.420744	53.307241	0.487981
55.655577	53.307241	0.607696
55.890411	53.307241	0.762228
56.125245	53.307241	0.756745
56.360078	53.307241	0.663581
56.594912	53.307241	0.669467
56.829746	53.307241	0.725943
57.064579	53.307241	0.745471
57.299413	53.307241	0.947467
57.534247	53.307241	0.820766
57.76908	53.307241	0.73286
58.003914	53.307241	0.766314
58.238748	53.307241	0.931504
58.473581	53.307241	0.969791
58.708415	53.307241	0.809409
58.943249	53.307241	0.778631
59.178082	53.307241	0.702378
59.412916	53.307241	0.566297
59.64775	53.307241	0.515766
59.882583	53.307241	0.719893
60.117417	53.542074	0.82124
60.35225	53.542074	0.465744
60.587084	53.542074	0.447471
60.821918	53.542074	0.695226
61.056751	53.542074	0.795614
61.291585	53.542074	0.786721
61.526419	53.542074	0.864656
61.761252	53.542074	0.881626
61.996086	53.542074	0.561798
62.23092	53.542074	0.45286
62.465753	53.542074	0.642777
62.700587	53.542074	0.902895
62.935421	53.542074	0.94104
63.170254	53.542074	1.026364
63.405088	53.542074	1.503767
63.639922	53.542074	0.65629
63.874755	53.542074	0.308041

136.9eV											
Spot	x (pixel)	Error x (pixel)	y (pixel)	Error y (pixel	radius (pixel)	error radius (pixel)	Radius m	Error radius m	Angle (Rad)	Angle degrees	Angle Error deg
1	1917.148	5.44	980.984	4.988	336.3648891	5.48079485	0.03072948	0.000515858	0.484310407	27.74894231	0.388848031
2	2059.917	3.543	1279.281	4.566	332.7413232	4.072573819	0.03039844	0.000391786	0.478651251	27.42469657	0.337874154
3	1870.778	5.017	1562.45	4.457	335.4589644	4.942359642	0.030646717	0.000468174	0.482893995	27.66778787	0.370164743
4	1539.673	5.989	1541.57	6.225	339.4729863	6.44405447	0.031013428	0.000601886	0.489177974	28.02783336	0.421104983
5	1393.835	3.94	1232.037	4.317	335.0458057	4.420920244	0.030608972	0.000422374	0.482248371	27.63079635	0.351473898
6	1575.277	3.851	955.383	3.587	339.7621868	4.107347993	0.031039849	0.000395617	0.489631529	28.05382011	0.341488325
Central											
x (pixels)	y (pixels)	Error x (pixel)	Error y (pixel)								
1727.795	1258.989	2.001	1.873								
Pixels per m	Error (pixel)	Screen distance (m)									
10946	44.2	0.066									
67.3eV											
Spot	x (pixel)	Error x (pixel)	y (pixel)	Error y (pixel	radius (pixel)	error radius (pixel)	Radius m	Error radius m	Angle (Rad)	Angle degrees	Angle Error deg
1	1350.424	6.969	1245.415	6.172	499.3255806	6.242851205	0.045617173	0.000403739	0.763105773	43.72274009	0.34400504
2	1693.021	8.017	1608.244	8.305	500.7036189	8.032472237	0.045743068	0.000502874	0.765748533	43.87415912	0.382789649
3	1549.583	6.248	2086.749	5.839	500.328069	6.035652282	0.045708758	0.000389865	0.76502765	43.83285558	0.337791624
4	1061.884	9.447	2193.782	8.644	491.9650264	8.715536526	0.044944731	0.000563518	0.749101106	42.9203318	0.407462214
5	738.789	6.462	1832.722	6.384	479.5768491	6.457969185	0.043812977	0.000430312	0.725932311	41.59285765	0.354761615
6	871.871	8.071	1374.06	7.589	483.1481606	7.822842771	0.044139244	0.000517972	0.732561781	41.97269829	0.396743204
Central											
x (pixels)	y (pixels)	Error x (pixel)	Error y (pixel)								
1205.719	1723.313	0.007	0.005								
Pixels per m	Error (pixel)	Screen distance (m)									
10946	44.2	0.066									

Figure 1 Data used to calculate the Bragg diffraction angles

Atomic Scale Characterization of Oxide Quasicrystal Thin Film by STM and LEED Proposal

Harry Hibbert 200983774

April 19, 2018

Supervisor: Dr. Hem Raj Sharma

Quasicrystals (QC) were discovered by Dan Schechtman in 1982 (Shechtman, Blech, Gratias, & Cahn, 1984). Crystal structures are highly ordered with long range orientational order with periodic spacing between unit cells. Quasicrystals are materials with long range translational order and long range orientational order. However, the translational order is not periodic and the structure does not have a rotational point symmetry (Levine & Steinhardt, 1986). A model of quasiperiodic tiling can be applied to QCs. A repeating motif fills space with unit cells or "tiles" in a way that maintains long range order without periodicity, a famous example is the Penrose tiling (Lifshitz, 2000). Surface science studies so far have tried to combine intermetallic QCs with common materials either by depositing single elemental adlayers on QC surfaces or by thin-film deposition of QC materials on periodic lattices. In 2013 Stefan Föster investigated a method of forming a two dimensional QC phase for the growth of $BaTiO_3$ with preferential pseudocubic structure of an elemental metal substrate with 3-fold symmetry. The experiment found that an aperiodic QC structure can be formed by annealing a $BaTiO_3(111)$ layer several monolayers thick on a Pt(111) substrate. On being annealed to 1,250K in a ultra high vacuum (UHV), the film restructures into a QC thin film. $BaTiO_3$ is a thoroughly investigated perovskite oxide and is also widely used in thin film applications and oxide heterostructures. In its paraelectric phase it crystallizes into a simple cubic lattice. As a result of matching lattice conditions it can be grown on many other perovskite substrates and also on metal substrates (Förster, 2013). This project will attempt to replicate this method to determine whether an aperiodic QC thin-film structure can derived from a periodic $BaTiO_3$ layer on a Ag single crystal substrate (instead of a Pt substrate) through analysis of low energy electron diffraction (LEED) and scanning tunnelling microscope (STM) images.

References

Förster. (2013). Quasicrystalline structure formation in a classical crystalline thin-film system. *Nature*, *502*(7470), 215.

Levine, D., & Steinhardt, P. J. (1986). Quasicrystals. i. definition and structure. *Physical Review B*, *34*(2), 596.

Lifshitz, R. (2000). The definition of quasicrystals. *arXiv preprint cond-mat/0008152*.

Shechtman, D., Blech, I., Gratias, D., & Cahn, J. W. (1984). Metallic phase with long-range orientational order and no translational symmetry. *Physical review letters*, *53*(20), 1951.

Week	***Description of Tasks***
1	Meet with Dr. Hem Raj Sharma to discuss the main precepts of the project and to have a tour of the surface science lab.
2	Become involved with the work of PhD students to gain further understanding of how surface science experiments are conducted and study the background required to understand the project. This includes UHV, surface crystallography, surface cleaning and the principles of LEED and STM. Submission of project proposal and risk assessment will take place this week.
3	Prepare Ag surface and $BaTiO_3$ for imaging.
4	Prepare the UHV for samples.
5	Take data of sample using LEED.
6	Take data of sample using STM.
7	Prepare project presentation. This will involve presenting the background theory of the project, motivations, the experimental methods and results found.
8	A presentation will be given to a group of peers and department of physics researchers.
9	Complete analysis of data for project report.
10	Work towards completing a first draft of the project report give a copy to Dr. Hem Raj Sharma so that he may review it.
11	Discuss the first draft with Dr. Hem Raj Sharma and make improvements where necessary.
12	Complete project report.

Table 1: A table showing the expected timeline of the project.